Exploring the Impact of Multivalent Substitution on High-Temperature Electrical Conductivity in Doped Lanthanum Chromite Perovskites: An Experimental and Ab-initio Study

Javier A. Mena[1*], Víctor Mendoza-Estrada[2], Edward M. Sabolsky[1], Konstantinos A. Sierros[1], Katarzyna Sabolsky[1], Rafael González-Hernández[2], Kavin Sivaneri Varadharajan Idhaiam[1]

[1]Department of Mechanical and Aerospace Engineering, West Virginia University, Morgantown, WV 26506, USA.
[2]Grupo de Investigación en Física Aplicada, Departamento de Física, Universidad del Norte, Km. 5 vía Puerto Colombia, Barranquilla, Colombia.

*Corresponding author: jam00009@mix.wvu.edu

Abstract

Doped $LaCrO_3$ perovskites hold promise as robust materials for electrical interconnects and sensor applications in harsh environments. In this work, we investigated the high-temperature behavior of $La_{1-x}Sr_xCrO_3$, $La_{1-x}Ca_xCrO_3$ and $La_{0.8}Sr_{0.2}Cr_{1-x}Mn_xO_3$ ($0.1 \leq x \leq 0.4$) through a combination of computational modeling and physical characterization up to 1500 °C. Crystalline structural properties were determined and compared with ab-initio calculations, which demonstrated excellent agreement with experimental findings. High-temperature electrical conductivity measurements were performed under different atmospheres. Calcium and strontium/manganese co-doped lanthanum chromites exhibited typical semiconductor exponential trends and conductivity showed proportional correlation with substitutions levels up to 30 %. The DFT modelling was completed up to 1500 °C, including low and high temperature chromite phases and oxygen vacancies insertion. Calculations were correlated with experimental electrical properties. This work expands the understanding of doped lanthanum chromites and paves the way for the development of materials suitable for demanding high-temperature applications.

Key words: Perovskite $LaCrO_3$, High-temperature conductivity, Solubility limit, Ab-initio calculations, Materials in extreme conditions

1. Introduction

Perovskite oxides ABO_3 materials have been studied in the past due their physical and chemical properties and potential technological applications in fields like heterogenous catalysis [1], superconductivity [2], optical materials light modulation [3], gas sensing [4] and solid-state electrolytes [5]. Cation substitution on the A- or B- site have been studied to understand and purposely tune the electrical, optical, magnetic, thermal, and structural properties [6-9]. $LaCrO_3$ is a particularly important perovskite material which is used in a variety of applications such as catalysis [10], high temperature electronics [11], energy storage [12] and in harsh environment sensing [13]. It is gaining an important place in such technological applications due to its refractory nature (high melting point ~ 2490 ºC) [14], electrical conductivity [15] and significant chemical stability under oxygen rich and reductive atmospheres [16]. To tune the $LaCrO_3$ physical properties, especially thermal expansion and electrical conductivity, various doping strategies which include A-site doping with alkaline earths, such a Ca, Sr, and Ba, and B-site doping with

transition metals such as Co, Ni, Fe, and Mn were completed [17-23]. These strategies typically resulted in modifications to their thermomechanical properties and the p-type semiconductor properties due to the dopant effects on the small polaron hopping mechanism and oxygen vacancy concentration [24, 25].

The initial volume of research on the $LaCrO_3$ composition was initiated in the 1980-90s, where these works focused on the effect of dopant type and concentration as related to the alteration of the electrical conductivity [26]. For example, the work by Mori et al. [27], showed that incorporation of divalent ions such as calcium and strontium increased the electrical conductivity significantly from 1.0 to 40.0 $S{\cdot}cm^{-1}$ and 1.0 to 36.6 $S{\cdot}cm^{-1}$ at 1000 °C, respectively. A few of these early papers also described the challenge in processing this refractory composition, indicating difficulty in producing phase purity when doping with alkaline earths and the effect of these A-site dopants on sinterability and grain growth processes (where the kinetics of both were enhanced with these doping schemes) [28]. There was increased focus on the composition starting in the early 2000s, and lasting for roughly a decade, where doped $LaCrO_3$ compositions were heavily considered as a potential ceramic solid-oxide fuel cell (SOFC) interconnect for high temperature operation to substitute for unstable metal interconnects at >700 °C [29-31]. The objective was to further increase the electrical conductivity of the composition, while at the same time, maintain an adequate coefficient of thermal expansion (CTE) near to that displayed by a typical SOFC electrolyte material (~10.5×10^{-6} /K for Y-stabilized ZrO_2, YSZ). Researchers dramatically increased their dopant approach to both A-site and B-sites within the structure, and further complex co-doping strategies were also attempted to balance out the sought requirements for SOFC interconnects within the application temperature range (700-850°C) [32]. Most of the publications focused on the $(La,Sr)CrO_3$ (LSC) composition, since it could be effectively co-doped with transition metals such as Co, Cu and V on the B-site to manipulate and improve the electrical conductivities with values of 58, 23.9, 9.7 S cm^{-1} at 1000°C and CTEs of 19, 9.81, 9.87 x10^{-6}/ °C, respectively [33]. Another well-researched co-doped $LaCrO_3$ composition was the $(La,Sr)(Cr,Mn)O_3$ (LSCM) composition with molar substitution levels between $0.1 \leq x \leq 0.3$ [26], where this composition was originally focused upon for SOFC interconnect applications, but later was found to be an interesting candidate for application as an anode electrode. The composition was found to adequately act as an oxidant catalyst for hydrogen and methane and was found to be stable in fuels containing low levels of sulfur that typically poison Ni-based SOFC anodes [34]. Interestingly, although there were many studies related to the effect of doping on electrical conductivity and thermal expansion as a function of temperature, the effects of the different working atmospheres on these two physical properties were limited (except for publications on the LSCM composition), even though this aspect was important to the SOFC interconnect application, where the interconnect is concurrently exposed to both oxidizing and reducing atmospheres [35]. The volume of research on the $LaCrO_3$ composition dramatically decreased over the past decade due to the push to lower the SOFC operating temperatures <700 °C to decrease cost and stability issues with active SOFC components (i.e., the electrodes) and other balance-of-plant materials. This transition in interest has eliminated the need for ceramic interconnects such as doped-$LaCrO_3$, where inexpensive and easy to process metals may be used.

As stated above, there is a considerable volume of literature available for the doped-$LaCrO_3$ composition related to the electrical conductivity and coefficient of thermal expansion up to roughly 800-900 °C in air for the SOFC application (and the related electrolyzer technologies), especially for the Sr-doped composition (LSC) and various co-doping strategies of this composition. However, there are very few reports on the electrical conductivity and stability of the doped-$LaCrO_3$ composition above this temperature range, even for the most common A-site doped compositions such as Sr and Ca. We are interested in the development of high-temperature sensors for application at temperatures >900 °C for various energy generation and conversion technologies, such as gas turbine, gasifier, and boiler technologies. High-temperature electrical conductors and interconnects are required for this temperature regime. In addition, these various applications also present very complex gas environments, where the partial pressure of oxygen can vary drastically, and thus, alter the electrical conductivity similarly. The objective of the current work was to explore for the first time the electrical conductivity of the typical Sr- and Ca-doped $LaCrO_3$ at the levels of 10-40 mol% up to 1500 ^oC under varying partial oxygen pressure atmospheres. The co-doped LSCM composition was also included due to the scientific interest, and breadth of publications, for this composition over the past decade. The phase development and stability were also investigated within this temperature range for these compositions by X-ray diffraction (XRD) and Rietveld methods. In addition, computational modelling methods were developed using new density functional theory (DFT) methods to investigate the effect of the dopant strategies on the high temperature properties, crystal structure, and stability.

2. Experimental

2.1 Lanthanum Chromite Ceramic Fabrication Method

All strontium, calcium and strontium/ manganese substituted lanthanum chromites ($La_{1-x}Sr_xCrO_3$, $La_{1-x}Ca_xCrO_3$ and $La_{0.8}Sr_{0.2}Cr_{1-x}Mn_xO_3$ ($0.1 \leq x \leq 0.4$)) compositions were synthesized by a modified Pechini sol-gel method employing citric acid (HO_2CCH_2-$C(OH)(CO_2H)CH_2CO_2H$) (99.9% purity) and $La(NO_3)_3 \cdot 6H_2O$ (99.9% purity), $Cr(NO_3)_3 \cdot 9H_2O$ (99.0% purity), $Sr(NO_3)_2$ (99.5% purity), $Ca(NO_3)_2$ (99.5% purity) and $Mn(NO_3)_2 \cdot xH_2O$ (99.0% purity) as metal sources (from Sigma Aldrich, USA). To simplify the nomenclature through this paper, compositions will be labelled as follows: LSC*x*, LCC*x* and LSCM*x* for strontium, calcium, and strontium/ manganese substitution respectively, where *x* indicates the percentage molar substitution level (10 - 40%).

All metal nitrates were dissolved in deionized water, and the accuracy of the final metal concentrations were established by an inductively coupled plasma- mass spectrometer (ICP-MS Perkin Elmer NexION 2000, USA) following the EPA Method 200.8. The required solution concentration of metal species for each studied composition were weighed and mixed with citric acid at an equivalent molar ratio of 1:2 (metal cations: citric acid). The solutions were heated to 80 ^oC to form a viscous gel which finally yielded a purple solid precursor during slow drying. The dried gel was then thermally treated at 400 ^oC for 1 h to remove the organic material. Samples were pulverized manually in a mortar and calcined at 900 ^oC for 5 h, where the perovskite phase was not formed yet at this temperature and the fine particle size of the precursor was retained.

These uncrystallized powders were then suspended in isopropyl alcohol (> 99%) and milled on a ball rolling system (US Stoneware 755RMV) using 3 mm ZrO_3-milling media for 2 h. The powders were dried, and the specific surface area of all powders were measured by using the BET method from the nitrogen adsorption isotherms obtained at liquid nitrogen temperature on a Micromeritics apparatus model ASAP–2000. Prior to the adsorption measurements, samples were routinely outgassed at 180 ^oC. The dense polycrystalline pellets of the powder were formed by initially uniaxially pressing under 1 MPa of pressure into circular pellets 50 mm diameter and approximately 5 mm thickness. The green bodies were sintered at 1600 ^oC with a heating rate of 2 ^oC/min under dry air with a holding time of 2 h, where a "reactive sintering" mechanism was completed. This term indicates that calcination to the full perovskite phase and the sintering mechanism occurs concurrently. The strategy is to maintain the finer particles size of the precursor materials to maintain the high driving force for densification. Bulk densities of the sintered pellets were measured by Archimedes method. Rectangular specimens, nominally 5 mm × 5 mm × 48 mm, were cut from the sintered circular pellets. Finally, the sintered rectangle-shaped pellets, that were used for electrical conductivity measurements for this study, were introduced into a high temperature furnace at 1000 ^oC with platinum wire contacts at predetermined distances. Platinum ink was used to coat contacts areas to reduce electrical resistance and to define the probe distances for the voltage and current.

2.2 Physical and Electrical Characterization Studies of Doped Lanthanum Chromite Ceramics

The phase purity of the prepared powders and sintered pellets were examined by X-ray diffraction (XRD, PANalytical *X'pert* PRO, Cu Kα radiation, model number PW 3040 Pro). Power requirements during the operation were 45 kV and 40 mA. The divergence slit angle for the incident X-ray beam was set to 0.5 º. Scans were performed with a 0.033 º/s scan rate and a 40 s step time. More detailed scans were performed using a 0.016 º/s scan rate and 400 s step time. X'Pert High Score software was used to identify the phases and crystal structure. In addition to the XRD analyses, quantitative phase analysis studies via Rietveld method were performed using the MAUD software [36] to determine the lattice parameters of synthetized materials. The microstructure of the sintered bodies was characterized using a Hitachi S-4700 Scanning Electron Microscope (SEM), using an accelerating voltage of 1–30 kV. Images were obtained in secondary electron mode at magnifications of up to 150000×. The pellet samples were polished to mirror-like surface, followed by thermal etching at 1550 ^oC for 15 min prior to SEM analysis. The electrical conductivities were measured using the DC four-probe method. The furnace temperature was measured with a calibrated R-type thermocouples. The first series of measurements were made in dry air. The second series of measurements were made under reductive atmosphere (using forming gas H_2:N_2 5 %: 95 % 200 cf, Matheson gas, West Mifflin, PA), all measurements were performed up to 1500 ^oC. Finally, conductivities measurements as a function of oxygen partial pressure were completed, regulating gas mixtures of Ar/O_2, where the oxygen partial pressure in the atmosphere was monitored by a zirconia oxygen sensor placed close to the sample. The oxygen partial pressure dependence was examined in the temperature range of 900-1500 °C with equilibrium times of 2 h between each measurement.

3. Theory/calculation

First-principles spin-polarized calculation within the density functional theory (DFT) framework were performed. Exchange and correlation effects were treated with generalized gradient approximation (GGA) and GGA+U method implemented in the Perdew-Burke-Ernzerhof functional (PBE) [37]. Constant effective parameter (U_{eff}) of 3.3 eV and 6.0 eV values were used for 3d orbitals of Cr and Mn atoms respectively. These values are supported by [38, 39] and describe the bulk electronic structure of pure and doped lanthanum chromite correctly, and therefore it is used in our calculations. The plane-wave projector augmented wave (PAW) method [40, 41] as implemented in Vienna Ab initio Simulation Package (VASP) [42, 43] was used. The electron wave function was expanded in plane waves up to a cutoff energy of 520 eV. 3×6×4 and 3×3×4 k-points mesh were employed for $2a\times1b\times1c$ and $2a \times 2b \times1c$ supercells based on a conventional $LaCrO_3$ (ABO_3) orthorhombic unit cell, as shown in Fig. 1 top. All the structures were relaxed until the total energy and residual force on each atom were less than 10^{-6} eV and 10^{-3} eV/Å, respectively. For consistent comparison to our experimental data for 10 – 40 % of A^{2+} = Sr, Ca (B^{3+} = Mn), two (One), four (two) and six (three) *La* (Cr) atom were replaced randomly by A^{2+} = Sr, Ca (B^{3+} = Mn) atoms to represent percentage substitution concentrations of x = 12.5 %, 25.0 % and 37.5 %, in $La_{1-x}Sr_xCrO_3$ (LSC*x*), $La_{1-x}Ca_xCrO_3$ (LCC*x*) and $La_{0.8}Sr_{0.2}Cr_{1-x}Mn_xO_3$ (LSCM*x*). For $LaCrO_3$, G-AFM ground state was found, for this total energy calculations were carried out for the ferromagnetic (FM) and three antiferromagnetic configurations (A-AFM, C-AFM and G-AFM) with the relaxed atomic positions, these results agree with the experimental and theoretical ones reported by other authors [44]. It has been reported that at room temperature pure $LaCrO_3$ exhibits an orthorhombic crystalline structure [44], and a phase transition to a rhombohedral structure has been observed around 600 K [45, 46]. In the same way the same orthorhombic to rhombohedral phase transition with the temperature increment was evidenced for divalent doped lanthanum chromite composition such as $La_{1-x}Sr_xCrO_3$ (LSC*x*) around 453 K [47-49] and $La_{1-x}Ca_xCrO_3$ (LCC*x*) for x = 0.00‑0.40 around 580 K and 824 K, respectively [50]. Considering the phase transition phenomena with the temperature increment in such compositions, the electrical conductivity (σ) was studied in this work for both orthorhombic and rhombohedral phases to compare the theoretical observations with the experimental results. σ was calculated using the BoltzTraP2 code [51] that is formulated according to classical Boltzmann transport equation under the constant relaxation time (τ) approximation. σ can only be obtained in units of τ, since there is no data available on the relaxation time on these materials. σ is 3 × 3 tensors for which the three diagonal elements correspond to transport along the cartesian x, y, and z directions. Therefore, we computed the scalar averages of σ using:

$$\sigma = \frac{1}{3}\mathrm{Tr}(\sigma) = \frac{1}{3}\left(\sigma_{xx} + \sigma_{yy} + \sigma_{zz}\right) \quad (1)$$

For an optimized rhombohedral structure, a similar calculation method other than the orthorhombic structure was considered, with a cutoff energy of 520 eV and 5×9×3 k-points mesh for $2a\times1b\times1c$ supercell. One, two and three *La* (Cr) atoms were replaced by A^{2+} = Sr, Ca (B^{3+} = Mn) atoms to represent percentage substitution concentrations of x = 8.33 %, 16.66 % and 25.00 %, in $La_{1-x}Sr_xCrO_3$ (LSC*x*), $La_{1-x}Ca_xCrO_3$ (LCC*x*) and $La_{0.833}Sr_{0.166}Cr_{1-x}Mn_xO_3$ (LSCM*x*) as shown in Fig. 1 bottom.

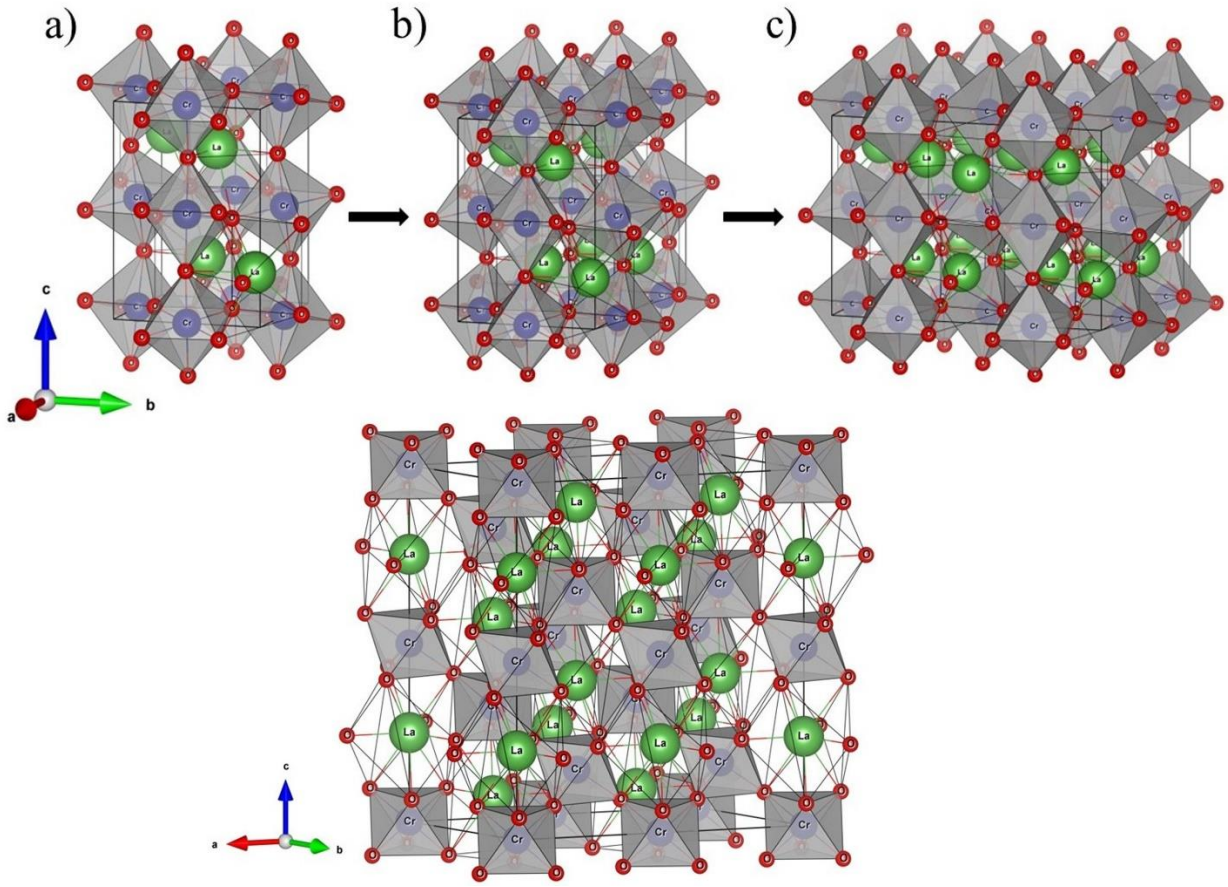

Fig. 1. **Top:** $LaCrO_3$ orthorhombic crystalline structure of **a)** Unit cell, **b)** 2a×1b×1c, and **c)** 2a×2b×1c supercell of $LaCrO_3$. **Bottom:** $LaCrO_3$ rhombohedral crystalline structure of 2a×2b×1c supercell.

4. Results and discussions

4.1 Phase and crystalline structure analysis

High density ceramic pellets were obtained by a reactive sintering process, as stated in experimental section, where fine particle size precursor powders calcined at 900 ºC (before the perovskite phase was completely formed) were pressed and sintered. Fig. S1 and Fig. S2 in the supplementary data section depicts the XRD patterns and pictures of Pechini sol-gel synthesis precursors calcined at different temperatures: 900 ºC, 1000 ºC, 1200 ºC and 1400 ºC. The XRD patterns of the produced strontium doped $LaCrO_3$ (LSC*x*) powders sintered at 1600 ˚C for 2 h are shown in Fig.2a. This figure indicates single phase formation for LSC40, LSC30, LSC20 and LSC10 (from top to bottom) defined by the high intense peaks that correspond to lanthanum chromite phase diffraction planes: (110), (112), (022), (004), (114), (024), (224), (143) and (332) (JCPDS card# 24-1016). This chromite phase has the orthorhombic perovskite structure with space group *Pnma* at room temperature as observed and reported previously for LSC*x*

compositions [52, 53]. The single-phase formation was also confirmed by the absence of characteristic peaks of constituent oxides for all the synthesized LSC*x* compositions. Fig.2b. illustrates a shift from left to right of the (110) crystallographic plane peaks of LSC*x* compositions as a function of the substitution level. Interestingly, the incorporation of strontium cations within the structure resulted in a gradual increasing shift of the two theta angles for all peaks due to cell contraction. However, contrary to the expected cell expansion associated with the larger Sr^{+2} ionic radius (1.44 Å) compared to the La^{+3} A-site's smaller ionic radius (1.36 Å) [54, 55], this unexpected contraction behavior can be attributed to the simultaneous B-site substitution of Cr^{+3} with Cr^{+4}, which possesses a smaller ionic radius than Cr^{+3}. Further elucidation of this phenomenon is provided later in the discussion. This observation and single-phase formation are evidence of the successful substitution of the strontium in the A-site of the lanthanum chromite perovskite crystalline structure.

Table 1 shows the experimental lattice parameters, unit cell volume, theoretical XRD density, and tolerance factor for the synthesized materials. The structural parameters were investigated and estimated by Rietveld refinement; the analysis confirmed an orthorhombic structure at room temperature for all studied compositions. This table indicates that according to the Rietveld analysis, the lattice parameters (*a*, *b* and *c*), unit cell volume, and crystallographic density magnitudes decreased, as a function of strontium substitution level increase for all LSC*x* materials. The calculated Goldschmidt tolerance factors (*t*) of 0.926, 0.947, 0.969, 0.992 for substitution molar percentage level of 10 %, 20 %, 30 % and 40 %, respectively, indicate how the increment of strontium content induces distortions into the perovskite structure without phase transitions ($0.8 \leq t \leq 1.0$). All these structural parameters decrement trends are explained by the oxidation of Cr^{+3} ion, and the formation of Cr^{+4} and Cr^{+6} ions as a result of the divalent cation (Sr^{+2}) substitution to achieve charge neutrality in the crystalline lattice. The altered valent chromium cation ionic radius of Cr^{+4} (0.50 Å) and Cr^{+6} (0.44 Å) [56] are smaller than the original Cr^{+3} ion size (0.62 Å) in the pure $LaCrO_3$ lattice, reducing in the lattice parameter. The observed divalent cation doping level correlation with the lattice parameter decrease was also observed and published by prior authors for Sr^{+2} [57], where LSC10 and LSC20 compositions were synthesized and found that higher substitution content correlates with smaller lattice parameters magnitude, unit cell volume and crystallographic density, in agreement with this work.

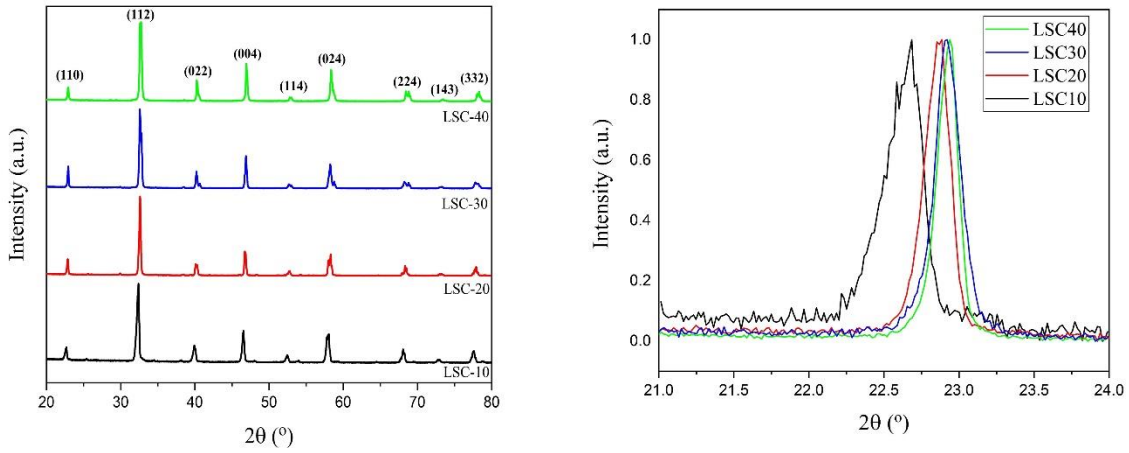

Fig. 2 XRD patterns of the produced strontium doped $LaCrO_3$ (LSC*x*) reactive sintered at 1600 ◦C for 2 h and shifting of (110) plane peak of LSC powder material evidencing the substitution on the lanthanum chromite perovskite structure.

Fig. 3 shows XRD patterns of the synthesized strontium/ manganese co-doped $LaCrO_3$ (LSCM*x*) compositions sintered at 1600 ◦C for 2 h using Pechini sol-gel method. As in the LSC*x* series, all LSCM*x* materials showed diffraction plane peaks that correspond to pure lanthanum chromite phase (JCPDS card# 24-1016): (110), (112), (022), (114), (024), (224), (143) and (332), and could be indexed as orthorhombic perovskite structure with space group *Pnma* at room temperature as observed and reported previously for LSMC*x* compositions previously by other authors [58-60]. However, single $LaCrO_3$ phase was observed for compositions substituted with manganese molar percentage up to 30% level, indicating the formation of the solid solution. For manganese molar percentage 40% content, splitting was observed on peaks: (022), (004), (114), (024), (224) and (332) suggesting the formation of a second perovskite as observed by [59]. Table 1 indicates how the increase of manganese content from 10 to 40 % (top to bottom in the LSCM*x* columns) correlates with the decrease of the lattice parameters *a*, *b* and *c*, in the same way with unit cell volume. However, the crystallographic density increases unlike the trend observed in only strontium substitution. The tolerance factor trend also shows an increase as a function of manganese substitution level. The decreasing trend in structural lattice parameters with increasing manganese molar percentage from 10 % to 40 % in LSCM*x* compositions can be explained by charge compensation for the Sr^{+2} presence in the structure, and the B-site cation oxidation for both the manganese and chromium ions: $Cr^{+3} \rightarrow Cr^{+4}$ and $Mn^{+3} \rightarrow Mn^{+4}$. This results in smaller cations on B-site reducing the lattice parameters, and in this case, the reduction of Mn^{+3} (0.64 Å) to Mn^{+4} (0.53 Å) [61] and Cr^{+3} (0.62 Å) to Cr^{+4} (0.50 Å) and Cr^{+6} (0.44 Å) was observed.

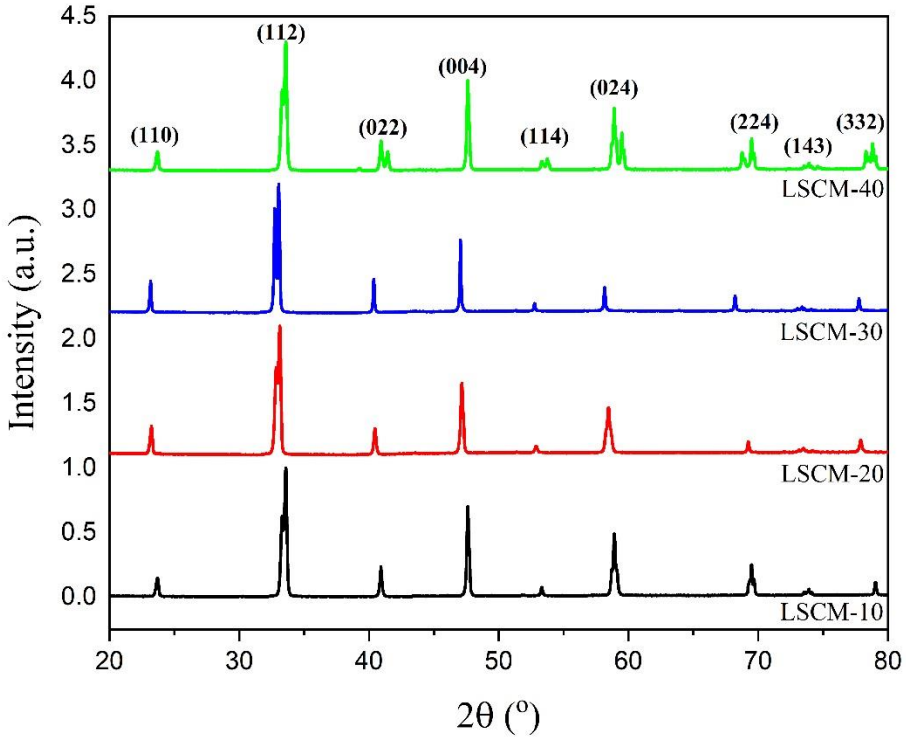

Fig. 3 XRD patterns of the produced strontium manganese co-doped $LaCrO_3$ (LSCM*x*) compositions reactive sintered at 1600 ◦C for 2 h.

Table 1 summarizes the structural parameters for all LCC*x* compositions synthesized. It is important to highlight that all the LCC*x* materials showed diffraction plane peaks that correspond to pure lanthanum chromite phase (JCPDS card# 24-1016): (110), (112), (022), (114), (024), (224), (143) and (332) and could be indexed as orthorhombic perovskite structure with space group *Pnma* at room temperature in agreement with the observations reported by [62]. It can be observed from the Rietveld analysis that the lattice parameters, unit cell volume, and crystallographic density decrease as a function of calcium substitution molar percentage levels from 10 % to 40 %. Tolerance factors correlate with calcium increment in the perovskite structure, with acceptable values ($0.8 \leq t \leq 1.0$), indicating that the structure is stable in the synthesized compositions. The decreasing structural trends, are explained by the fact that the introduction of Ca^{+2} in the La^{+3} position, produces the same structural effects as discussed for Sr^{+2}; where charge compensation leads the equimolar formation of Cr^{+4} whose ionic radius is smaller than Cr^{+6} cations. However, the decrease in lattice parameters is also related to the smaller ionic radius of Ca^{+2} (1.34 Å) [56] in comparison with La^{+3} (1.36 Å). The observed divalent cation doping level correlation with the lattice parameter reduction was also observed and published by prior authors for Ca^{+2} [63, 64] where higher substitution content correlates with smaller lattice parameters magnitude, which agrees with the results with this work.

Table 1 Experimental Lattice Parameters, Unit Cell Volume, Crystalline XRD Density and obtained by X-ray Diffraction Patterns for sintered LSC*x*, LSCM*x*, and LCC*x* Compositions.

Composition	Lattice parameters (Å)			Volume ($Å^3$)	$\rho XRD_{Theoretical}$ (g/cm^3)	Tolerance Factor (*t*)
	a	c	b			
LSC10	5.512	7.792	5.566	239.129	6.493	0.926
LSC20	5.498	7.785	5.542	237.274	6.400	0.947
LSC30	5.476	7.758	5.523	234.683	6.326	0.969
LSC40	5.452	7.740	5.512	232.644	6.235	0.992
LSCM10	5.473	7.776	5.564	236.859	6.420	0.921
LSCM20	5.470	7.770	5.558	236.282	6.444	0.937
LSCM30	5.459	7.749	5.539	234.402	6.504	0.953
LSCM40	5.414	7.706	5.498	229.422	6.654	0.971
LCC10	5.418	7.733	5.503	230.605	6.596	0.904
LCC20	5.409	7.726	5.498	229.789	6.334	0.903
LCC30	5.399	7.705	5.487	228.326	6.087	0.902
LCC40	5.389	7.685	5.462	226.252	5.853	0.901

Fig. 4 shows the linear correlation between the doping percentage of Sr, Mn, and Ca in the $LaCrO_3$ perovskite structure, and the volume cell divided by Z (where Z indicates the number of $LaCrO_3$ by unit cell, which in this case is 4), aiming to assess the adherence of each system to Vegard's law [65]. The figure consists of three sub-graphs, each representing different compositions of LSC*x*, LCC*x*, and LSCM*x*. In the LSC*x* system, a linear correlation between doping levels and unit cell volume change is evident, showcasing a decrease in cell volume as strontium content increases. For instance, with strontium percentages of 10%, 20%, 30%, and 40%, the respective cell volumes are 59.78 $Å^3$, 59.33 $Å^3$, 58.68 $Å^3$, and 58.14 $Å^3$. This trend adheres to Vegard's law, supported by an R^2 coefficient of 0.998. Similarly, in the LCC*x* system, increasing calcium content correlates with a reduction in cell volume, with volumes of 57.85 Å3, 57.45 $Å^3$, 57.03 $Å^3$, and 56.58 $Å^3$ for calcium percentages of 10%, 20%, 30%, and 40%, respectively, confirming compliance with Vegard's law (R^2 = 0.997). However, in the LSCM*x* system, an unexpected trend emerges: despite increasing manganese content, cell volume decreases, indicating a departure from Vegard's law. For manganese percentages of 10%, 20%, 30%, and 40%, cell volumes are 59.20 $Å^3$, 59.06 $Å^3$, 58.59 $Å^3$, and 57.36 $Å^3$, respectively, with an R^2 coefficient of 0.864. It is very important to highlight that the graph distinctly portrays Vegard's law compliance for the first three cell volume values (59.20 Å, 59.06 Å and 58.59 Å) corresponding to manganese contents of 10%, 20%, and 30%, respectively. However, with a 40% manganese content, Vegard's law is violated, possibly due to the formation of a second phase of isostructural perovskite with a different composition, which also was clearly discernible in the X-ray diffraction analyses (see Fig. 3).

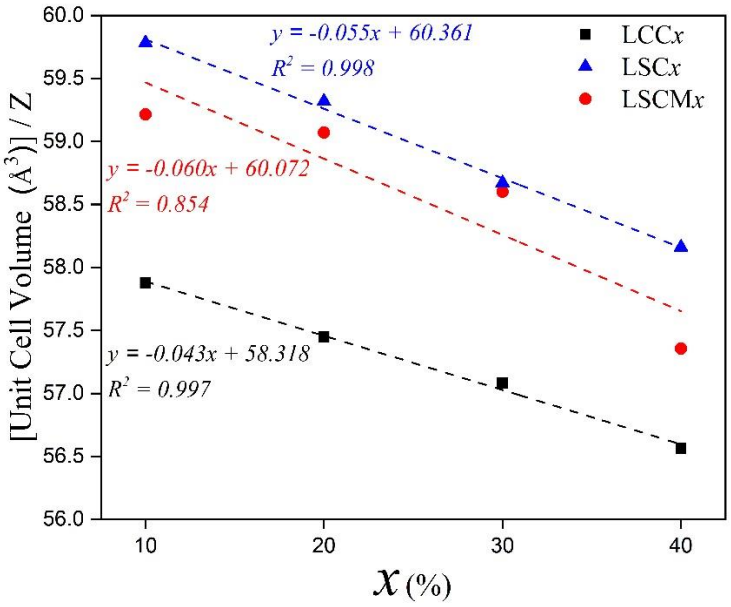

Fig. 4 Unit cell volume/number of formula units in the unit cell (Z) in function of dopants molar substitution percentage for LSC*x*, LSCM*x* and LCC*x*.

To better understand the effects produced by ionic substitution on the physical properties, DFT calculations were performed. There are few DFT theoretical works reported for singular doped lanthanum chromites materials, and their structural and electrical properties at low temperatures [66]. However, there is not a combined systematic analysis for a range of LSC*x*, LSCM*x* and LCC*x* compositions, especially to the elevated temperature range. In this current work, we performed the first DFT calculations using molar percentage substitution levels from 10-35 mol% (more specifically, 12.5 %, 25.0 % and 37.5 %) for strontium, calcium, and manganese. Considering that these materials experience crystalline phase transitions between low and high temperatures, and to obtain a more accurate modeling of the electrical conductivity trends, calculations were performed assuming both the orthorhombic and rhombohedral phases within both the low and high temperature ranges, respectively, as explained in the theory/calculation section.

Table 2 shows the DFT calculated lattice parameters, unit cell volume, theoretical density, and the average absolute local magnetization (for the Cr and Mn atoms) for the doped lanthanum chromites perovskites with GGA+U, where U = ($U_{eff\text{-}Cr}$ = 3.3 eV and $U_{eff\text{-}Mn}$ = 6.0 eV). In this table, it can be observed that for the LSC*x* compositions, the lattice parameters, unit cell volume and density magnitudes decrease as strontium molar substitution level increase. For all strontium substitutions levels, we found that the average magnetic moments of the Cr ions decrease with respect to the magnetic moment of chromium in pure lanthanum chromite. This is also theoretical evidence of the chromium ions oxidation from Cr^{3+} to Cr^{4+}, as suggested in the experimental discussion. The trending correlation between strontium content increase and the lattice parameters was observed in the experimental results (see Table 1), as well as the DFT calculations. The substitution of Sr^{+2}

in La^{+3} sites produced the equimolar formation of Cr^{+4} for charge neutrality in the structure. Structurally, the changes in lattice parameters are related to the ionic radius of Cr^{+3} (0.62 Å) to Cr^{+4} (0.50 Å), as explained above.

Table 2 also shows the theoretical structural data for LSCM*x*, where it can be observed how the increase in manganese content produced a slight increase in the *a*, *b* and *c* lattice parameters of the lanthanum chromite perovskite structure; however, it is not clear that a trend can be correlated with the manganese content. The unit cell volume for 12.5 % was found to be 234.41 $Å^3$, for 25.0 % reduced to 234.25 $Å^3$ and finally with 37.5 % increased to 234.90 $Å^3$. The average absolute magnetic moment for chromium increased as a function of manganese content. Finally, the calculated lattice parameters, unit cell volume, and crystalline density for LCC*x* compositions exhibited an inverse proportional correlation with calcium molar substitution level from 12.5 % to 37.5 %. It is clearly observed that lattice parameters were reduced in magnitude. The chromium average absolute magnetic moment also decreased as evidence of the incorporation of calcium in the structure. As compared with experimental data for LCC*x* in Table 1, the observed correlation with cation substitution levels was the same. As with Sr^{+2}, the introduction of Ca^{+2} produced an equimolar formation of Cr^{+4} in the perovskite B-site, reducing in the dimension of the lattice. To visualize the trends shown in Table 2, Fig. S3 in the supplementary material shows the theoretical DFT and XRD estimated lattice parameters dependence with the dopant molar percentage in LSC*x***,** LSCM*x* and LCC*x*. Fig. S3 a-c shows that DFT calculated lattice parameter trends agree with the experimental measurements in the approximated molar percentage range studied by the implementation of this modeling approach; however, an inherent slight variability in such ranges could be easily observed. For LSC*x* (Fig. 5a), the calculated parameters *a*, *b*, and *c* exhibited a magnitude overestimation relative to the XRD results with 0.05 Å, 0.01 Å, and 0.08 Å, respectively. On the other hand for the LSCM*x* (Fig. 5b), it can be observed that for the parameters *a*, *b,* and *c*, their magnitude values were overestimated by 0.04 Å, underestimated by 0.06 Å and slightly variated by 0.02 Å, respectively; finally, for LCC*x* (Fig. 5c) the three parameters *a*, *b* and *c* ranges exhibited a magnitude overestimation of 0.08 Å, 0.04 Å and, 0.08 Å, respectively. This magnitude variability is generally observed in DFT calculations, determining the contribution of the pseudopotential's suitability versus the impact of the optimization procedure at T = 0 K on such variability remains challenging. This issue is also evident in the structural optimization of perovskite phases, as underscored by this investigation. However, these theoretical values validate the dopant configuration selected for the supercell's construction. It is important to highlight that even while the selected theoretical dopant percentage concentration values exhibit slight differences (attributable to the constraints inherent in the construction of the supercells within the theoretical framework), they were chosen to closely approximate the compositions utilized in the experiments.

Subsequently, considering the Cr^{+3} and Cr^{+4} ionic size, the Goldschmidt tolerance factor *(t)* was calculated to establish the theoretical degree of lattice distortion for the studied systems. It is very important to highlight that those calculations were done using a modified tolerance factor relation, considering that divalent dopant concentration in the A-site is equivalent to Cr^{+4} concentration in the B-site. The Goldschmidt tolerance factor is defined by [67]:

$$t = \frac{r_{Aeff} + r_O}{\sqrt{2}(r_{Beff} + r_O)} \qquad (2)$$

Where the effective ionic radius of A cation is calculated from the relation:

$$r_{Aeff} = (1 - x)r_A + xr_{doping\ ion} \quad (3)$$

$$r_{Beff} = (1 - x)r_{Cr^{3+}} + xr_{Cr^{+4}} \quad (4)$$

With respect to our DFT+U calculation, the terms $r_{Aeff} + r_O$ and $r_{Beff} + r_O$ were considered as the average bond lengths between A-O and B-O atoms, respectively. The estimated tolerance factors reported in Table 1 and Table 2, show that substitution and doping levels did not affect the lattice structural properties (acceptable *t* values are between 0.8-1.0), maintaining in this way, the pure original lanthanum chromite perovskite structure.

Table 2. DFT Calculated Lattice Parameters, Unit Cell Volume, Density, and Average Absolute Local Magnetization using GGA+U, where U = ($U_{eff\text{-}Cr}$ = 3.3 eV and $U_{eff\text{-}Mn}$ = 6.0 eV).

Composition	Lattice Parameters (Å)			Volume ($Å^3$)	Density (g/cm^3)	$\|M_{Cr}\|$ (μ_B)	$\|M_{Mn}\|$ (μ_B)	Tolerance Factor (*t*)
	a	b	c					
$LaCrO_3$	5.557	5.593	7.871	244.637	6.486	2.803	-----	0.908
LSC12.5	5.550	5.558	7.882	243.165	6.351	2.722	-----	0.922
LSC25.0	5.532	5.549	7.871	241.599	6.215	2.641	-----	0.927
LSC37.5	5.522	5.502	7.868	239.961	6.080	2.503	-----	0.934
LSCM12.5	5.512	5.482	7.758	234.415	6.416	2.422	2.464	0.947
LSCM25.0	5.510	5.482	7.755	234.260	6.431	2.517	2.452	0.949
LSCM37.5	5.533	5.493	7.729	234.906	6.424	2.53	2.680	0.944
LCC12.5	5.526	5.559	7.861	241.460	6.232	2.72	-----	0.907
LCC25.0	5.497	5.532	7.840	238.415	5.967	2.64	-----	0.910
LCC37.5	5.463	5.503	7.823	235.159	5.701	2.51	-----	0.907

4.2 Microstructure characterization after sintering for the doped-$LaCrO_3$ compositions

The microstructure of the sintered pellets for each composition was examined by polishing the top surface down to a depth of ~1 mm (to a roughness of 0.6 μm), and then completing scanning electron microscopy (SEM) of this surface after thermal etching. The samples were thermally etched at 1550 ^oC in dry air for 15 min before rapid cooling. Fig. 5 (a-c) shows the SEM micrographs of LSC20, LSCM20, and LCC20, respectively, after thermal etching at 1550 ^oC in

dry air. Fig. 5a shows that LSC*x* sintered pellets microstructure consisted of a bimodal grain size distribution with a population of isometric grains of ~5 µm in size, which coexisted with smaller grains with a size <2.0 um (resulting in an average grain size of ~3.5 um). A population of intergranular porosity was observed with a similar size distribution. Table 3 summarizes the average grain size, bulk density and BET surface area (for the starting powder) for the LSC*x*, LSCM*x* and LCC*x* compositions. In this table, it is shown how the surface area of the starting powder had a surface area ranging between 2.1-3.5 m^2/g for all compositions, where there was a slight decreasing trend in surface area (or increase in average particle size) with increasing dopant concentration. This trend is consistent with results reported previously for divalent ions doping [68, 69] causing a slight increase in particle size during calcination processes due to enhance diffusivity. In the same way, it can be observed that there is a proportional correlation between relative density and substitution level. It is clear that by increasing the dopant concentration results in an increase in the densification process. A maximum relative density of 97 % theoretical density was achieved for the LSC*x* samples. It is important to remark that typically reported densities are below 90 % [28, 68]; only a very few authors have reported higher densities with values ~96 % (where the powder was synthesized by approaches such as hydrothermal and combustion methods) [63, 69]. Generally, divalent cations such as Ca^{2+} and Sr^{2+} were proper candidates to increase densification of lanthanum chromite [70], and thus, improve physical properties such as mechanical strength and electrical conductivity [71]. The table also shows that for these compositions the average grain size of the sintered structures was ~3.8 um. Fig. 5b displays the strontium and manganese co-doped lanthanum chromite, which exhibits a similar trend as the strontium substitution, with grains of average size of ~3.5 um and some remaining porosity. Table 3 shows how increasing the manganese concentration increased the bulk density values from 95 % to a maximum of 97 %. As observed for LSC*x* and LCC*x* compositions, the surface area magnitude decreased as substitution concentration increased.

Fig. 5c exhibits that the LCC*x* compositions pellets show a denser microstructure, where the porosity is reduced significantly in comparison with LSC*x* and LSCM*x*. The LCC*x* microstructure shows equiaxial grains with an average size of ~3.8 um. Table 3 shows that by increasing the calcium content in the lanthanum chromite structure, the bulk density increases with values from 96 % to a maximum of 98 % of theoretical density. Generally, it was found that with the higher calcium concentrations, the relative density increased, and the porosity decreased for LCC*x* materials, as well as the surface area magnitude decreased. A few other researchers showed a similar higher densification for higher calcium concentrations (≥ 20 mol %) and it was associated to a fine level of liquid phase sintering, which promoted higher diffusivity through the grain boundaries [72, 73]. This phenomenon also promotes the enhanced grain growth that produces the larger size grain [74].

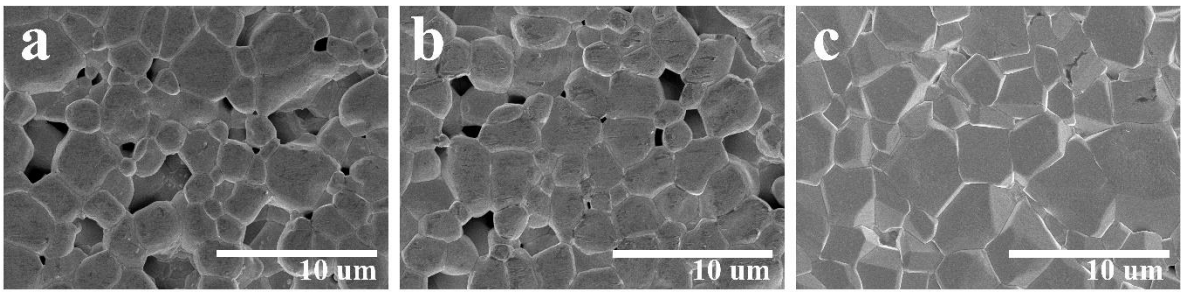

Fig. 5 SEM micrograph of samples **(a)** LSC20, **(b)** LSCM20 and **(c)** LCC20 reactive sintered at 1600 ^{o}C for 2 h in air.

Fig. 6 shows the SEM images of these ceramics with the effects of the divalent cation substitution levels on densification and sintering. In Fig 6a, it can be observed that there is higher porosity in LSC20 in comparison with LSC30 (seen in Fig 6c). By increasing the strontium content from LSC20 to LSC30, the porosity was reduced, and a larger grain size was achieved as shown in Fig. 6b and Fig. 6d. Similar results were observed by [72, 75], where the strontium doping enhanced the densification of lanthanum chromites considerably from 70 % to >85 % of relative density for pure $LaCrO_3$ and Sr-doped $LaCrO_3$, respectively.

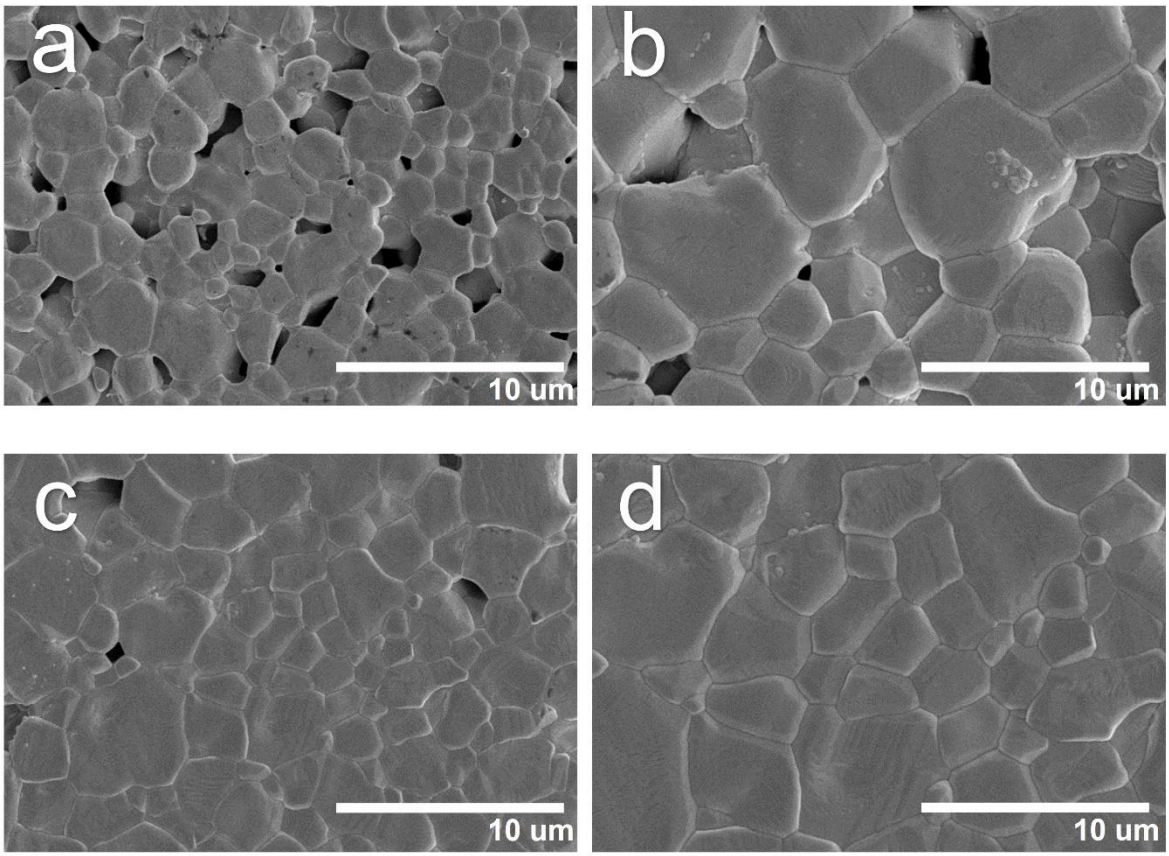

Fig. 6 SEM micrograph of samples **(a-b)** LSC20, **(c-d)** LSC30 sintered at 1600 ^{o}C for 2 h in air.

All the LSC*x*, LSCM*x* and LCC*x* synthesized by the stated sol gel method exhibited higher sinterability under oxidizing conditions with observed relative densities in the range between 94-98% as reported in Table 3. These densities are considerably higher in comparison with pure $LaCrO_3$ which was densified previously to a relative density of 85 % [64]. The densification of multivalent cations doped lanthanum chromites was found to change significantly, depending not only on the substitution level, but also in the synthesis approach.

Table 3 Average Grain Size, Bulk Density and BET Surface Area for LCC*x*, LSC*x* and LSCM*x* Compositions.

Composition	S_{BET} ($m^2 g^{-1}$)	Relative Percentage Bulk Density (%)	Average grain length (μm)
LSC10	3.1	94	3.6
LSC20	2.9	95	3.4
LSC30	2.8	97	3.6
LSC40	2.0	97	3.2
LSCM10	3.0	95	3.3
LSCM20	2.7	96	3.5
LSCM30	2.4	96	3.5
LSCM40	2.1	97	3.4
LCC10	3.5	96	3.7
LCC20	3.4	97	3.8
LCC30	3.2	97	4.1
LCC40	2.8	98	3.7

4.3 Electrical conductivity characterization

Fig 7. shows the experimental temperature dependence of the electrical conductivity of LSC*x*, LSCM*x* and LCC*x* under oxidizing atmosphere measured by DC four-probe measurements. Taking into account the different temperature ranges where the transitions from orthorhombic to rhombohedral phase occur, each subgraph is divided into three regions, for each of the studied compositions. The estimated temperature ranges where the orthorhombic and the rhombohedral regions are predominant are highlighted as a blue and/or pink areas, respectively. The phase transition region is shown as a green striped colored area, representing a broader temperature range estimated for the orthorhombic-rhombohedral transition based on previously reported values, since the accurate ranges are not still well-defined in literature. For the LSC*x* composition, this range was considered between 30 ^{o}C – 180 ^{o}C; for LSCM*x*, it was considered to be 260 ^{o}C – 280 ^{o}C; and for LCC*x*, it was considered as 306 ^{o}C – 560 ^{o}C. Fig.6a shows LSC*x* electrical conductivity correlation with temperature. The figure shows that for all strontium substitution levels (10 - 40 %), the electrical conductivity remained constant until 700 ^{o}C, then it was observed to increase as a function of temperature until 1200 ^{o}C, where again the magnitude remained constant up to 1500 ^{o}C. Table 4 shows the electrical conductivity values at 1000 ^{o}C under oxidizing atmosphere conditions. As shown in the table, the magnitude increased proportionally with strontium up to 30 % substitution content as observed in all LCC*x* and LSCM*x* compositions. In contrast with LCC*x* materials, the Ca^{+2} 10 % doping level showed lower conductivity than the same strontium doping level (at 1000 ^{o}C); however, the Ca^{+2} 30 % doping level displayed a higher conductivity and good stability in the whole temperature range. The reason for the higher conductivity in the Ca-doped $LaCrO_3$ composition is related to the radius of Ca^{+2} (1.34 Å) which is closer to the host ion radius,

La^{+3} (1.36 Å), as compared to that of Sr^{+2} (1.44 Å). This is shown by the smaller lattice parameters of the LCC*x* materials in comparison with LSC*x* and LSCM*x* (see Table 1), which permits a more efficient polaron hopping process, because the lattice experiences a lower distortion through the lattice, and thus, higher mobility of the charge carriers.

The LSC*x* compositions exhibited a different electrical conductivity behavior in the whole working temperature range in contrast with LCC*x*. In order to understand this phenomenon, the LSC20 and LCC20 compositions were annealed for 5 h under air atmosphere at different temperatures from 800-1200 ºC (by increments of 100 ºC), then XRD measurements were performed on each composition. Fig. S4 in the supplementary data section showed the XRD spectra for LSC20 after the heat treatments. The series of XRD spectra showed the formation of a strontium chromate secondary phase. For the same series of experiments, the XRD data for LCC20 (in Fig. S5 within the supplementary section) showed that no new secondary phase was formed during heating at this temperature range. In one previous work [76] found in literature, it was shown that an occasional secondary strontium chromate phase was formed for strontium doping levels x = 0.15, 0.20, 0.30, 0.50 after annealing at ~ 950 ºC for 2 h. These results are evidence that strontium presents a lower solubility limit and higher mobility than calcium within the $LaCrO_3$ composition. The formation of a secondary phase in LSC*x* materials helped explain the difference in the electrical conductivity trends in contrast with the LCC*x* and LSCM*x* compositions.

Fig. 7b shows the electrical conductivity under oxidizing atmosphere conditions up to 1500 ºC for LSCM*x* compositions. It can be observed that an exponential correlation between electrical conductivity and temperature exists. The electrical conductivity magnitude correlates proportionally with the manganese content increase from 10% to 30% in the entire working temperature range. For the highest substitution level of 40%, the electrical conductivity magnitude decreased. Table 4 reports the activation energies of the electrical conductivity up to 1500 ºC. An inverse correlation with the substitution level increase was the same observed for all LCC*x* compositions. A decrease was observed in manganese concentration between 10-30 %. The electrical conductivity values for LSCM*x* compositions were smaller than those observed for all LCC*x*; substitution of Cr^{+3} in the B-site by Mn^{+3} decreased the electrical conductivity magnitude according to prior observations. Manganese ions present a different electronic structure than chromium [73]; Mn^{+3} ions have a partially filled conduction band as opposed to Cr^{+3} filled band. The conduction in these materials occurs primarily in conduction band of Mn^{+3} and there is no evidence of polaron hopping between Cr sites, since Mn substitutes the Cr in the crystalline structure, inhibiting in this way the transition from Cr^{+3} to Cr^{+4}. The charge compensation by the presence of divalent Sr^{+2} produces the oxidation of Mn^{+3} to Mn^{+4} in the B-site or oxygen vacancies formation. Previous authors proposed that the higher activation energies at lower Mn^{+3} concentrations are associated with large separation of the manganese ions [77]. In the opposite way, increasing the Mn^{+3} molar substitution level produced a decrease in the activation energy due to Mn ions separation distance decrease. This observation agrees with our estimated activation energies reported in Table 4 [78].

Fig. 7c shows the LCC*x* compositions electrical conductivity dependence with temperature, it was observed that all LCC*x* compositions showed an exponential correlation between electrical

conductivity and temperature in the range up to1500 ^{o}C; it can be observed that the electrical conductivity magnitude correlates proportionally with the calcium substitution level increase from 10 % to 40 % in the entire temperature range. Table 4 summarizes the electrical conductivity and activation energies under oxidizing and reducing atmospheres for LCC*x*, LSC*x* and LSCM*x* compositions. Activation energies of electrical conduction were computed from the slope of the least squares fit of log *(σT)* against *(1/T)* using the linearization form of the Arrhenius relation:

$$log(\sigma T) = log\sigma_0 - \left(\frac{\Delta E_a}{kT}\right) \quad (5)$$

Where σ is the electrical conductivity, σ_0 is the pre-exponential factor related to the charge carrier density , ΔE_a is the activation energy, *k* is the Boltzmann constant and *T* the absolute temperature. Even though the measurements were completed for temperatures up to 1500 ^{o}C for the first time, the electrical conductivity measurements data at 1000 ^{o}C were displayed to compare with previous work by Mori *et al.*, to standardize the initial and intrinsic performance of the studied compositions [27]. In Table 4, it can be observed how the electrical conductivity values at 1000 ^{o}C for the LCC*x* compositions increase proportionally with calcium content from 10 % to 30 %; however, at 40 % the electrical conductivity did not follow the observed correlation, showing a lower magnitude. In the same way, the activation energies decreased from 0.142 eV to 0.103 eV between calcium content of 10 % to 30 %. This observation indicates that increasing the calcium molar substitution level results in a decrease in the activation energy. The plots show how the lanthanum site substitution with Ca^{+2} increased the electrical conductivity magnitude under oxidizing atmosphere up to ≤ 30 % doping levels. This increase has been attributed to the equimolar formation of Cr^{+4} as the result of charge compensation by the divalent ion substitution, producing in this way electrical conduction by the polaron hopping between the Cr^{+3} and Cr^{+4} chemical species. In pure $LaCrO_3$, the electrical conductivity mechanism is based on the cation vacancies formation and positive electron hole compensation, producing in this way small polaron hopping. The positive hole transport can be expressed by the reaction using the Kroger-Vink notation:

$$\frac{3}{2}O_2 \leftrightarrow V_{La}''' + V_{Cr}''' + 3O_o^{\times} + 6h^{\bullet} \quad (6)$$

Where V_{La}''' and V_{Cr}''' indicate cation vacancies, $O_o^{\times}$ is the oxygen site and $h^{\cdot}$ positive holes. For divalent substituent compositions (LCC*x* and LSC*x*), the introduction of divalent cation is compensated by the oxidation of Cr^{+3} to Cr^{+4} at high oxygen pressures (10^{-8}atm), to achieve electrical neutrality both systems should meet the conditions $[Sr_{La}'] = [Cr_{Cr}^{\cdot}] = [Cr_{Cr}^{+4}]$ and/or $[Ca_{La}'] = [Cr_{Cr}^{\cdot}] = [Cr_{Cr}^{+4}]$, respectively. At 40% doping level, the conductivity decreased; previous observations reported by Devi *et al*., suggest that for high divalent ions doping levels (≥ 35%) charge compensation may take place by the creation of oxygen vacancies, reducing electrical conductivity and increasing ionic conduction in the structure [75].

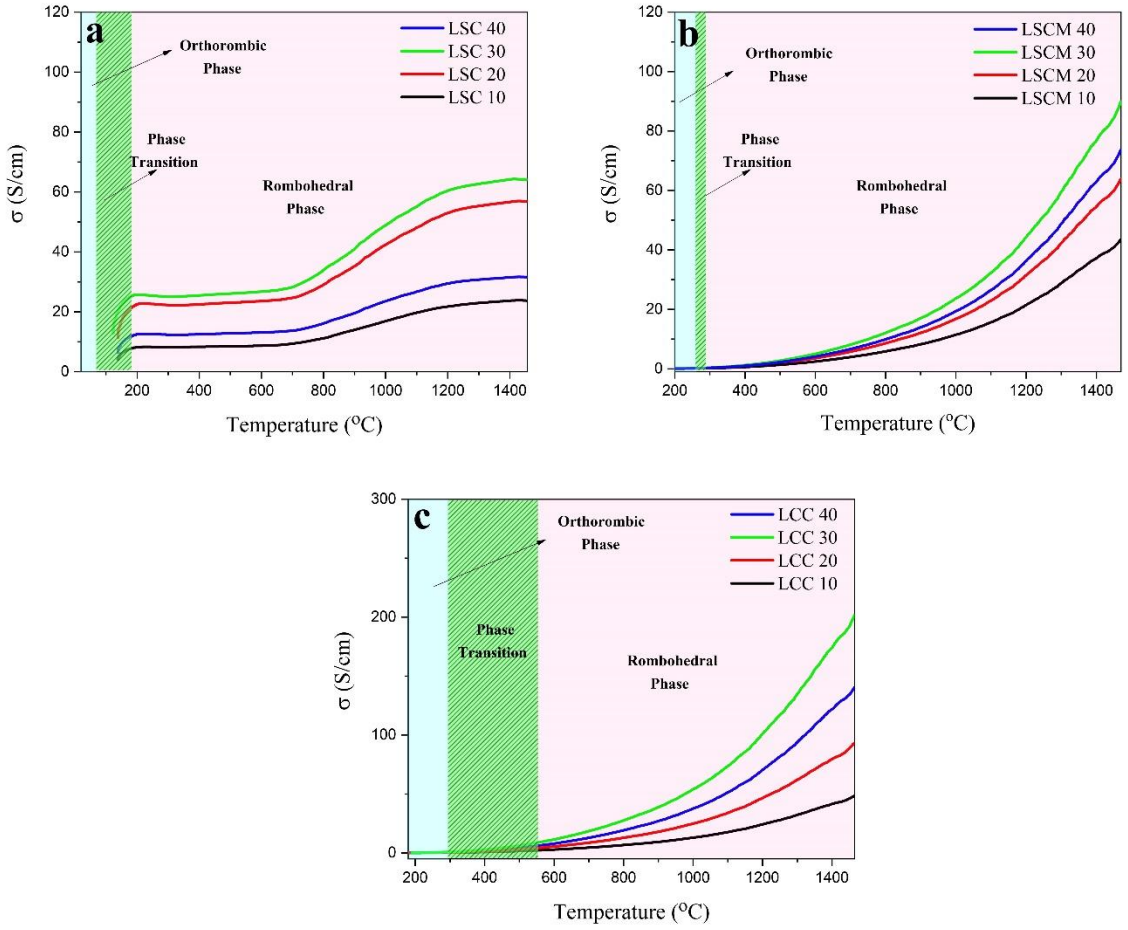

Fig. 7 Experimental temperature dependence of the electrical conductivity of **(a)** LSC*x*, **(b)** LSCM*x* and **(c)** LCC*x* under oxidizing atmosphere conditions (green area indicates the orthorhombic to rhombohedral phase transition temperature range).

Table 4 Electrical Conductivity and Activation Energies under Oxidizing and Reducing Atmospheres for LSC*x*, LSCM*x* and LCC*x* Compositions.

Composition	Air Atmosphere		Reducing Atmosphere	
	Conductivity @ 1000 °C (S/cm)	Activation energy (eV)	Conductivity @ 1000 °C (S/cm)	Activation energy (eV)
LSC10	16.67	0.16	2.69	0.32
LSC20	42.88	0.14	4.57	0.26
LSC30	49.03	0.11	5.53	0.17
LSC40	23.60	0.15	3.46	0.31
LSCM10	10.22	0.14	0.28	0.56
LSCM20	16.36	0.14	2.10	0.33
LSCM30	56.84	0.11	8.69	0.18
LSCM40	24.99	0.13	4.00	0.15
LCC10	13.21	0.14	3.15	0.32
LCC20	24.17	0.13	4.12	0.21
LCC30	52.82	0.10	7.60	0.14
LCC40	38.15	0.12	6.63	0.18

Fig. 8 shows the electrical conductivity versus temperature for LSC*x*, LSCM*x* and LCC*x* compositions under reducing atmosphere conditions. Fig. 8a shows the LSC*x* electrical conductivity correlation with temperature under reducing conditions. It can be observed that as Fig. 7a showed for all strontium substitution levels (10 % - 40 %) the electrical conductivity remains constant until 700 °C, and then the trend increased near linearly until the temperature of 1150 °C, where again, it returned to a constant value with increasing temperature. Table 4 shows that the reducing conditions electrical conductivity values at 1000°C, increased proportionally with strontium content level up to 30 %. However, comparing electrical conductivity values under reducing conditions with those measured under oxidizing atmosphere, it was evidenced that a decrease in magnitude was measured for all the characterized compositions. This observation is explained by the reduction of Cr^{+4} ions to Cr^{+3} and the formation of oxygen vacancies for charge compensation due the presence of Sr^{+2} cations in the A-site . These electrical conductivity values at 1000 °C agreed with a previous work [33], where Ca^{+2} and Sr^{+2} were used as A-site substituent in $LaCrO_3$ perovskite and tested under both oxidizing and reducing conditions.

In the same way, Fig. 8b shows an exponential trend for the electrical conductivity versus temperature throughout the entire temperature range for the LSCM*x* compositions under reducing atmosphere. The LSCM10 exhibits a low conductivity that slightly increased for LSCM20 and achieved maximum values for the LSCM30 sample. However, for the LSCM40 composition, the electric conductivity slightly decreased below LSCM30; these conductivity trends at 1000 °C can be observed with detail in Table 4; such table also shows the activation energies trends for LSCM*x*. The activation energy decreased proportionally with Mn content up to 30% as expected. Generally, under reducing conditions the electrical conductivity magnitude was lower than the overall magnitudes shown for the compositions in the oxidizing atmospheres measurements. The decrease in the electrical conductivity can be explained by the reduction of both Cr^{+4}/ Mn^{+4} to Cr^{+3}/ Mn^{+3}

in the B-site and the formation of oxygen vacancies to achieve electrical neutrality. Finally, in Fig. 8c, it can be observed that the increase in calcium content in the lanthanum perovskite structure increased the electrical conductivity values as seen before in Fig. 7c under an oxidizing atmosphere, where an exponential correlation was measured. The electrical conductivity dependence with calcium content in LCC*x* under reducing atmosphere is shown in Table 4, where the conductivity magnitude increased proportionally with calcium molar concentration up to 30 %. However, as observed for LSC*x* and LSCM*x* under reducing conditions, the conductivity magnitude decreased by one order of magnitude when compared with values observed in oxidizing atmosphere. Activation energies decreased as a function of calcium content but increased in contrast to oxidizing atmosphere. The electrical conductivity exponential behavior trend was observed under both oxidizing and reducing atmospheres in the same temperature working range, indicating that the LCC*x* compositions are chemically stable under oxidizing and/or reducing conditions. Under the reducing atmosphere, the materials experienced a reversible charge compensation by the reduction of Cr^{+4} to Cr^{+3}, because the presence of substitute divalent cation, oxygen vacancies are formed to achieve electrical neutrality as expected, decreasing in this way the electrical conductivity magnitude by the increase of ionic conduction mechanism.

Fig. 9 shows electrical conductivities in comparison at 1000 ^{o}C for LSC*x* and LCC*x* ($0.1 \leq x \leq 0.3$) reported for this work and by Mori *et al*. [27]. This previous work was the only one found in literature to report calcium and strontium substituted lanthanum chromite with same molar substitution levels. In this figure, it can be shown that for this work, and for that previously reported, the measured electrical conductivity were similar in order of magnitude. It is important to highlight that the connecting lines between points in Fig. 9 are not actual measured data, they were added as visual guidelines to show the electrical conductivity dependence with substitution concentration trends.

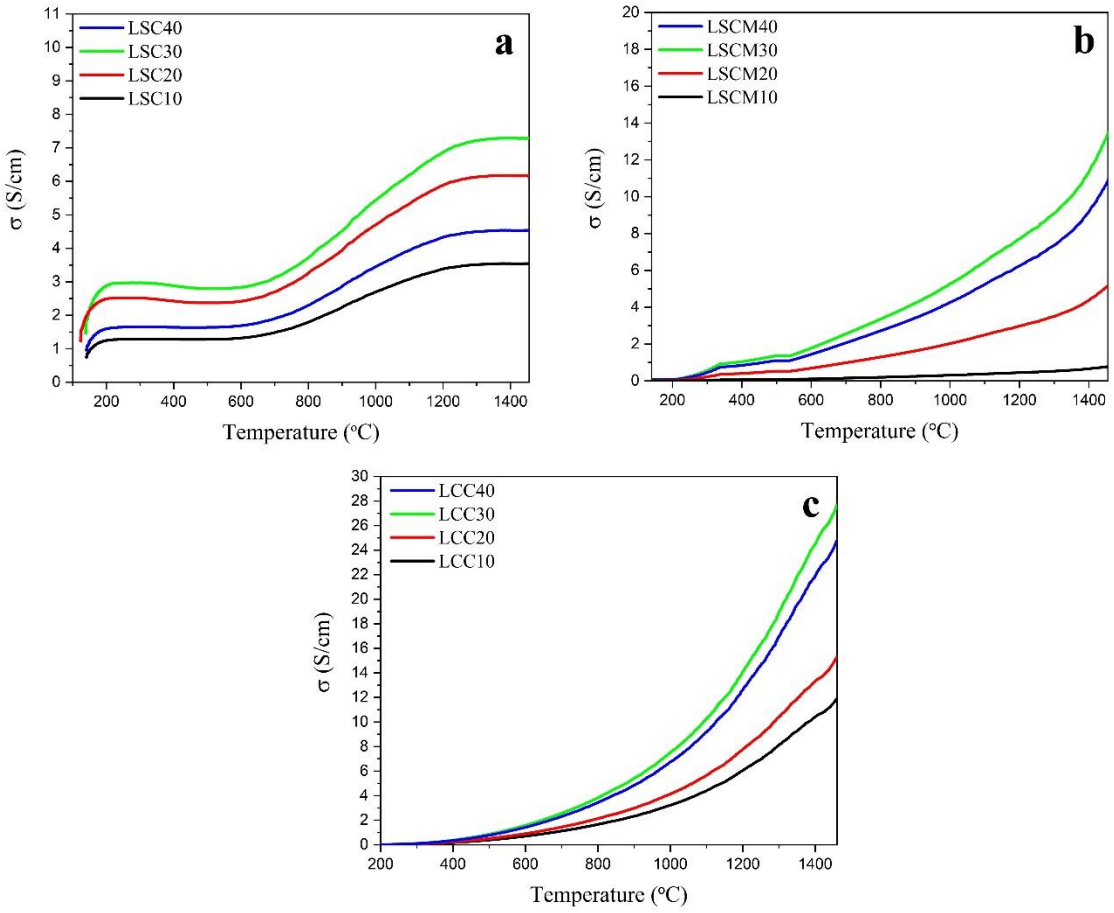

Fig. 8 Electrical conductivity versus temperature for **(a)** LSC*x*, **(b)** LSCM*x* and **(c)** LCC*x* compositions under reducing atmosphere conditions.

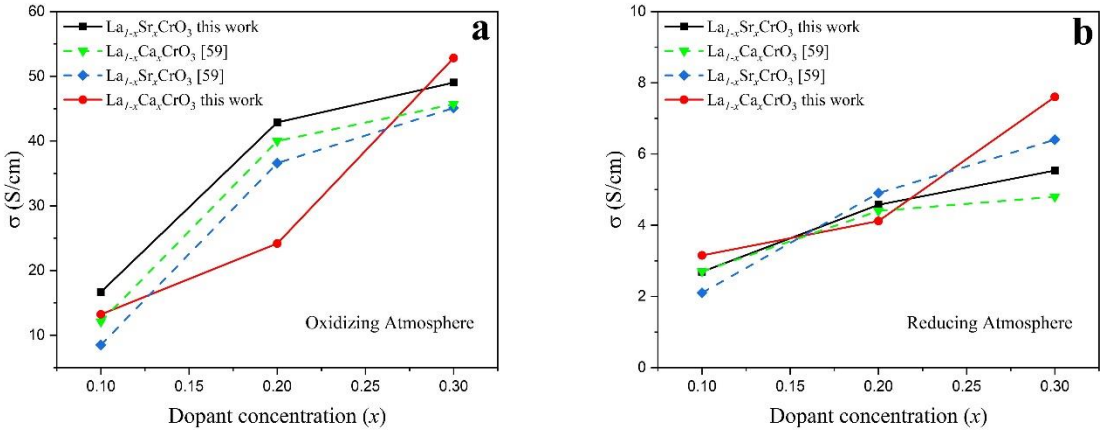

Fig 9 Electrical conductivities at 1000°C for LCC*x* and LSC*x* ($0.1 \leq x \leq 0.3$) under **(a)** oxidizing and **(b)** reducing atmospheres determined on this work and by Mori *et al.*, [27].

Fig.10 compares the electrical conductivity isotherm under different oxygen partial pressures (P_{O2}) for the LCC*x* compositions at 900 ºC, 1200 ºC and 1500 ºC. It can be seen again that the increase in calcium content correlates proportionally with the increase in the electrical conductivity. At higher P_{O2} (> 10^{-14} atm) the conductivity in all the temperatures presented a constant value independent of P_{O2}. One important observation is that the width of this conductivity in the P_{O2} non-dependent region decreases with increasing calcium content and at higher temperatures. However, at $P_{O2} \leq 10^{-12}$ atm, a critical point is achieved where the conductivity decreased exponentially as a function of P_{O2} as shown for all LCC*x* compositions, evidencing a p-type semiconductor behavior. This electrical conductivity drop is compensated by an ionic conduction mechanism due to oxygen vacancy formation and decrease in positive holes concentration by the reduction of Cr^{+4} to Cr^{+3} and a constant concentration of Ca^{+2} substituent cation. At lower oxygen partial pressures, the conductivity decreases exponentially for divalent doped $LaCrO_3$ as reported by various authors [79, 80]. This phenomenon was explained by the formation of oxygen vacancies to compensate the presence of divalent dopant cations in low oxygen activity regions ≤ 10^{-14} atm and can be expressed using Kröger-Vink notation by the reaction [33]:

$$\frac{1}{2}O_2 + V_O^{"} + 2Cr_{Cr}^{\times} \leftrightarrow O_O^{\times} + 2Cr_{\dot{C}r} \quad (7)$$

Under variable oxygen partial pressure or reducing atmosphere conditions, to achieve electrical neutrality for the systems, $La_{1-x}Sr_xCrO_{3-\delta}$ and $La_{1-x}Ca_xCrO_{3-\delta}$ should meet $[Sr'_{La}] = 2V_O^{"} + [Cr_{\dot{C}r}]$ And/or $[Ca'_{La}] = 2V_O^{"} + [Cr_{\dot{C}r}]$ [79]. The effect of temperature in the electrical conductivity for all the studied LCC*x* compositions can be seen with the increase in magnitude from 900 ºC to 1500 ºC, as expected.

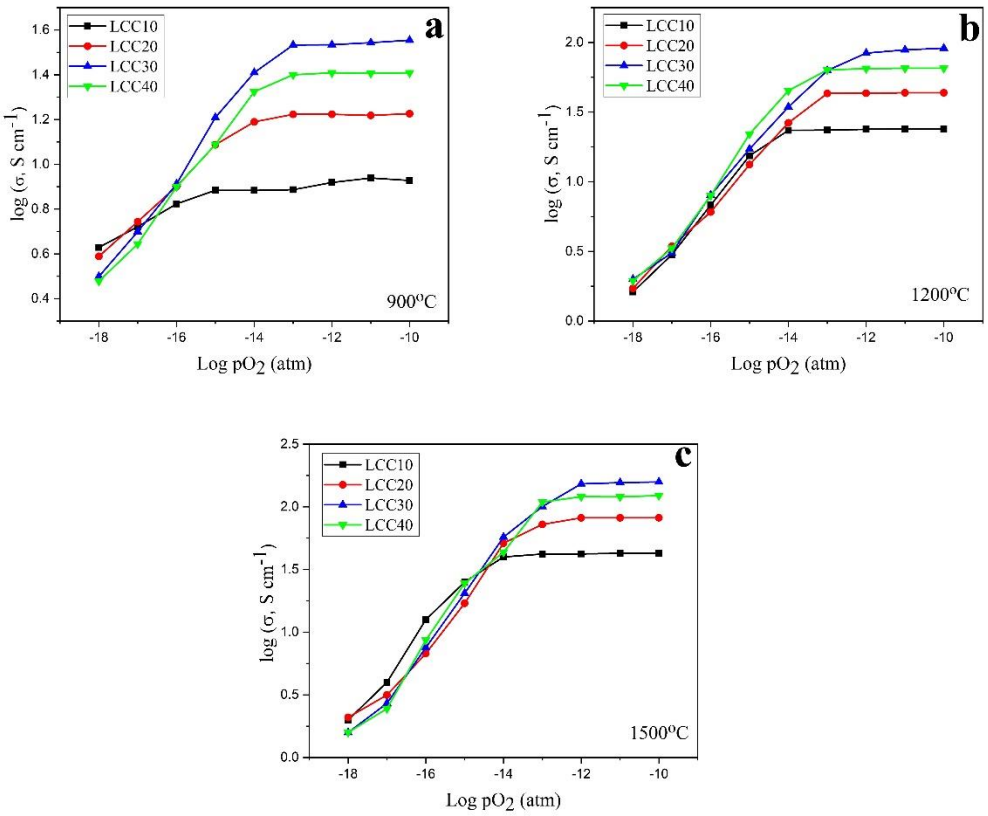

Fig. 10 Oxygen partial pressure dependence of electrical conductivity at **(a)** 900 ºC, **(b)** 1200 and **c)** 1500 for LCC*x* compositions.

Fig. 11 shows the oxygen partial pressure (P_{O2}) dependence of the electrical conductivity and different working temperatures for LSC10, LSC20 and LSC30 compositions. For all studied temperatures (600 ºC, 900 ºC, 1200 ºC and 1500 ºC), there exists a critical P_{O2}value where the conductivity mechanism changed (which causes an exponential decrease of the electrical conductivity). At lower temperatures, the critical P_{O2}value decreased. At 1500 ºC, the critical partial pressure is ~ 10^{-14} atm and for 900 ºC is ~ 10^{-17} atm. At lower temperatures, the electrical conductivity dominates the contribution, and at higher temperatures the ionic conduction is more notable. The high temperature condition facilitates the oxygen vacancies formation, producing a decrease in positive holes concentration; this explains the low electrical conductivity trend in all compositions. It was observed that at lower temperatures (600 – 900 ºC), no significant changes in conductivity occurred for strontium doped compositions during the equilibrium time used (120 min). At higher temperatures (1200 ºC and 1500 ºC), the conductivity dropped exponentially at lower oxygen partial pressures. Increasing the strontium concentration, the conductivity decreased faster and significantly because of the formation of oxygen vacancies. For all LSC*x* compositions and at all temperatures, conductivity is independent of oxygen partial pressure in the high Po_2 region above about 10^{-12} atm. Generally, in the low Po_2 region ($\leq 10^{-14}$ atm), the electrical conductivity was strongly dependent on the oxygen partial pressure and its magnitude decreased due to ionic compensation, where it became the dominant mechanism through the formation of

oxygen vacancies. This observation agrees with the point defect model used by [80, 81] as results of their oxygen non-stoichiometry of LSC*x* thermogravimetric study.

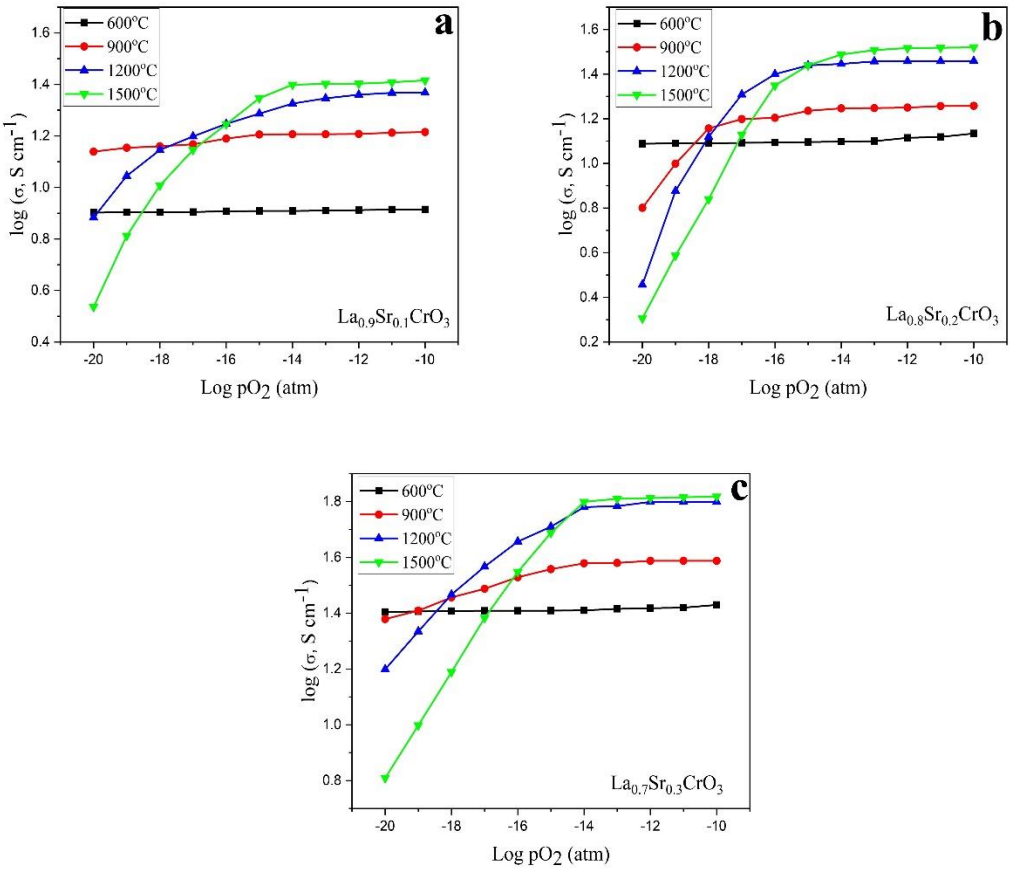

Fig. 11 Electrical conductivity under different oxygen partial pressures and working temperatures for **(a)** LSC10, **(b)** LSC20 and **(c)** LSC30 compositions.

4.4 First principles DFT modelling

In order to analyze the experimental and theoretical effects of cationic substitution type, concentration, and operation temperature on electrical conductivity, the DFT calculations were performed to incur a deeper understanding of the observed trends. As indicated previously in the paper, only a few DFT theoretical works were previously reported in literature for substituted lanthanum chromites and their electrical properties [82, 83], but these works did not consider a large dopant range (and alternate dopant types) and limited the calculations to lower temperature (as reflected in the experimental work completed in this work). In this way, these works did not study the effects of crystalline phase transitions (orthorhombic to rhombohedral structure) on such electrical properties at high temperatures.

The initial DFT model focused on the substitution of only the divalent cation (Sr^{+2} and Ca^{+2}) substitution on the A-site within the perovskite structure, with the formation of positive holes due to the oxidation of chromium from Cr^{+3} to Cr^{+4}, as discussed previously. In the first theoretical modelling results (not shown in this work), the doped chromites showed a metallic behavior without the formation of oxygen vacancies, which agrees with a previous results published by [82]; however, the materials studied in this work do not exhibit metallic behavior according to the electrical conductivity measurements (and other experimental works [83, 84]). The experimental works show that the divalent cation substitutions do not undergo the insulator-to-metal transition even at the maximum possible extent of hole doping [85]. Therefore, to lead to the insulating state, it was assumed in our calculations that oxygen vacancies were formed; when two La^{3+} ions are substituted by two Sr^{+2} or Ca^{+2} ions, one oxygen atom is removed forming an oxygen vacancy (V_o). Fig. 12 shows the oxygen vacancy formation and polaron localization at the vicinity Cr-O octahedra for LSC12.5 and LCC12.5. It can be seen for both composition schematics, the formation of oxygen vacancy (dotted circles) and the simultaneous bonds distortion between oxygen (red) and chromium atoms (blue) that lead the small polaron localization specifically around Cr^{4+} ions, which electronic density distribution is also shown (green lobules). The substitution of La^{+3} ions by divalent cations and oxygen vacancies formation cause the formation of polarons lying near the vacancy. The formation of this polar state with the excess charge localized at single Cr atoms is accompanied by a modification of the structural distortions around the polaronic sites. Cr^{+4} is strongly attracted to neighboring O atoms, contracting the bonding length to 1.88 Å; while the attraction of Cr^{+3} atoms and O atoms is weaker, leading to increased Cr^{+3}–O bond length to ~2.00 Å. The charge carrier transport could occur by hopping between adjacent localized states.

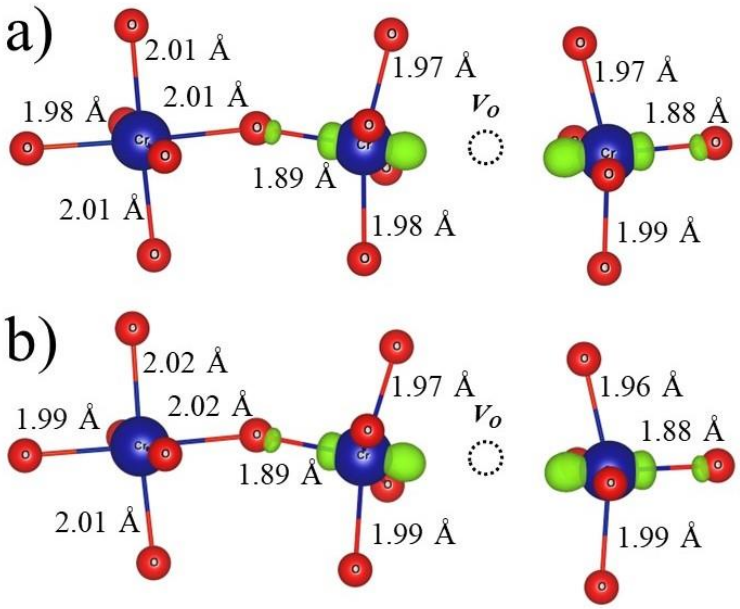

Fig. 12 Polaron localization (green lobules) and oxygen vacancy (dotted circles) formation at the vicinity Cr-O octahedra in **(a)** LSC12.5 and **(b)** LCC12.5. Oxygen and chromium atoms are represented by red and blue spheres, respectively.

To perform comparable DFT modelling with the experimental observations for room temperature conditions, the orthorhombic crystalline structure was considered [39]. In the case of the high temperature conditions, the rhombohedral phase was used. The maximum phase transition temperature from orthorhombic to rhombohedral phase was previously reported for $LaCrO_3$, $La_{1-x}Sr_xCrO_3$ and $La_{1-x}Ca_xCrO_3$ to be 580 K [40, 41], 453 K [42-44] and 730 K [45], respectively. DFT calculations were performed for both the orthorhombic and rhombohedral phases independently to compare within the appropriate (*phase valid*) temperature range. The orthorhombic phase modelling used molar percentage substitution levels x = 12.5%, 25.0% and 37.5% in $La_{1-x}Sr_xCrO_3$ (LSC*x*), $La_{1-x}Ca_xCrO_3$ (LCC*x*) and $La_{0.8}Sr_{0.2}Cr_{1-x}Mn_xO_3$ (LSCM*x*). The rhombohedral structure modelling was performed using substitution levels x = 8.33 %, 16.66 % and 25 %, in $La_{1-x}Sr_xCrO_3$ (LSC*x*), $La_{1-x}Ca_xCrO_3$ (LCC*x*) and $La_{0.833}Sr_{0.166}Cr_{1-x}Mn_xO_3$ (LSCM*x*). Fig. 13 shows the DFT theoretical electrical conductivity over the relaxation time (σ/τ) as a function of temperature for the rhombohedral structure (Fig. 13 a-c) and the orthorhombic (Fig. 13 d-f) for LSC*x*, LSCM*x* and LCC*x* compositions. This figure indicates individually for each substituent cation and its concentration levels. Each of these subgraphs is divided into three regions, taking into account the different temperature ranges where the transitions from orthorhombic to rhombohedral phase occur for each of the studied compositions: (*i*) the *"valid"* region shows the theoretical regime where the phase used in the DFT modelling is suggested to be stable ; (*ii*) the *"invalid"* region where the phase used in that specific DFT modeling is not stable; (*iii*) the *"phase transition"* region, shown as a green striped colored area, representing a broader temperature range estimated for the orthorhombic-rhombohedral transition based on reported values reported by other researchers for the range of dopant concentrations and types (Sr , Sr/ Mn, Ca). For the LSC*x* composition, this range was considered between 30 ^oC – 180 ^oC; for LSCM*x*, it was considered to be 260 ^oC – 280 ^oC; and for LCC*x*, it was considered as 306 ^oC – 560 ^oC.

It is important to highlight that the numerical values of the electrical conductivity as a function of temperature obtained in the DFT modeling are not directly comparable with the experimental results, because the magnitudes of these theoretical values depend on the relaxation time (τ), as previously mentioned in the methodology for the DFT model developing and application. However, to make an estimated analysis between the theoretical values and experimental observations of conductivity, the activation energies and pre-exponential factors of each set of data (theoretical and experimental) were determined for each substituent cation composition set, using the linearized conductivity's Arrhenius function (equation 5). Table 5 summarizes such values obtained for the DFT modeling for both the orthorhombic and rhombohedral phase, in the *valid* and *invalid* regions. In the same way, this table summarizes the activation energies and pre-exponential factors for the experimental data. All the temperature dependence of the electrical conductivity Arrhenius plots for the experimental measurements, rhombohedral phase, and orthorhombic phase DFT modelling can be found in the supplementary section in Fig. S6, Fig. S7 and Fig. S8, respectively.

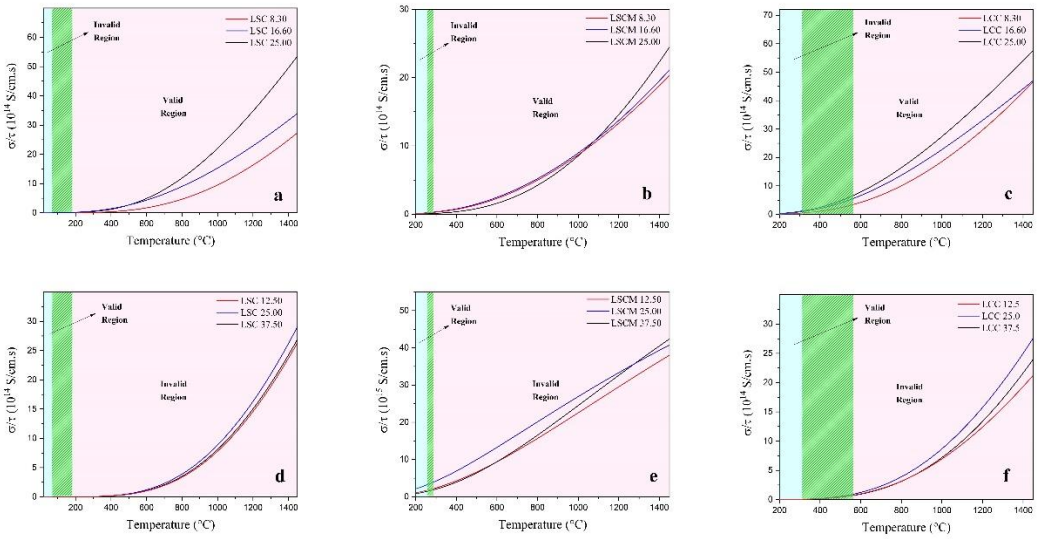

Fig 13 DFT theoretical electrical conductivity dependence with temperature when the rhombohedral phase **(a-c)** and orthorhombic phase **(d-f)** were assumed within the DFT model for the LSC*x*, LSCM*x* and LCC*x* compositions.

As previously discussed, in the high temperature regime, the differently doped lanthanum chromite compositions exhibit a rhombohedral phase. Considering the relevance of the theoretical information on the behaviors and trends of electrical conductivity as a function of the substituent cation, concentration level, and its correlation with the working temperature at high magnitudes regimes, the discussion will initially focus on the results of the DFT modeling for the rhombohedral crystalline phase. Initially, Fig. 13a shows (σ/τ) trends as a function of temperature for the different compositions of lanthanum chromite doped with Sr (with the *valid region*). In each of the three plots that correspond to each level of substitution of Sr (8.30 %, 16.60 % and 25.00 %) on the La A-site, an exponential increase in conductivity is observed as temperature value increases. Relative to the concentration of the substituent, the magnitude of (σ/τ) increases proportional to the Sr content in the lanthanum chromite perovskite. There is an equimolar relationship between the concentration of the substituent cation and the concentration of positive holes in this type of p-type semiconductor. The increase in sites for electron hopping and the simultaneous formation of polarons result in the reduction in activation energy as observed in Table 5 for both theoretical and experimental results. On the other hand, the pre-exponential factor that is related to the density of charge carriers increases as a function of the concentration of Sr as predicted by the polaron hopping model. and as mentioned before, there is a proportional increase between the content of Sr and the density of charge carriers. Comparing the theoretical behavior of the dependence on the temperature of the conductivity with the experimental trends in Fig.7a, it was possible to verify that although the same correlation is observed between the concentration of Sr and the increase in conductivity, there is no agreement between the conductivity behaviors of both groups of data. As previously discussed, Sr tends to move through the lanthanum chromite lattice, forming a secondary phase of strontium chromate with increasing temperature. This displacement of Sr

generates oxygen vacancies to maintain the charge neutrality of lanthanum chromite, thus generating the experimentally evidenced behavior. The DFT model does not predict the formation of secondary phases and how this phenomenon influences the behavior of conductivity.

The case is different for the Sr/Mn co-doped system, shown in Fig.13b, where there is an exponential increase in (σ/τ) as a function of both temperature and Mn content (within the *valid region*). As the concentration of Mn increases, a slight increase in conductivity was observed. Table 5 shows that by increasing the concentration of Mn (and thus, the conductivity), the activation energy of (σ/τ) decreases 0.212 eV, 0.175 eV and 0.172 eV for Mn content of 8.3%, 16.0% and 25.0%, respectively, indicating that the increase in substitution concentration results in the more conductive material. The same activation energy dependence with Mn content reduction was observed for the experimental observations on LSCM*x* (*x*= 10.0-30.0%) compositions. The calculated exponential trends between temperature and conductivity agreed with the experimental data, as well as the increase of its magnitude as a function of Mn increase, as observed in Fig.7b.

Finally, Fig.13c shows that for the LCC*x* composition with the rhombohedral phase (within the *valid region*), similar results were calculated as within the other modelled systems, where the trend displays an exponential temperature dependence for σ/τ. It can be observed that a proportional increase in the conductivity as a function of Ca content was identified, as summarized in Table 5, and with that trend, the activation energy magnitude decreased due to the increase in hole concentration and polaron formation.

Table 5 Activation energies and pre-exponential factors for the DFT modelling and experimental electrical conductivity dependence with temperature for LSC*x*, LSCM*x* and LCC*x* Compositions.

DFT modelling data									
	Orthorhombic structure					Rhombohedral structure			
Composition	Valid		Invalid		Composition	Invalid		Valid	
	$\Delta E\ (eVs^{-1})$	$log\sigma_0$	$\Delta E\ (eVs^{-1})$	$log\sigma_0$		$\Delta E\ (eVs^{-1})$	$log\sigma_0$	$\Delta E\ (eVs^{-1})$	$log\sigma_0$
LSC 12.50	0.25	5.64	0.18	5.34	LSC 8.30	0.15	5.12	0.18	5.77
LSC 25.00	0.22	5.81	0.16	5.95	LSC 16.00	0.10	6.62	0.17	5.88
LSC 37.50	0.24	5.71	0.12	5.60	LSC 25.00	0.12	6.23	0.14	5.99
LSCM 12.50	0.32	5.01	0.17	5.55	LSCM 8.30	0.12	5.16	0.19	5.65
LSCM 25.00	0.27	5.16	0.15	5.63	LSCM 16.00	0.11	5.17	0.18	5.71
LSCM 37.50	0.29	5.03	0.14	5.74	LSCM 25.00	0.13	5.41	0.17	5.99
LCC 12.50	0.31	5.80	0.16	6.20	LCC 8.30	0.15	5.59	0.19	6.06
LCC 25.00	0.26	5.95	0.14	6.33	LCC 16.00	0.14	5.61	0.18	6.16
LCC 37.50	0.28	5.87	0.14	6.32	LCC 25.00	0.13	5.64	0.17	6.25

Experimental data				
	Orthorhombic structure		Rhombohedral structure	
	$\Delta E\ (eV)$	$log\sigma_0$	$\Delta E\ (eV)$	$log\sigma_0$
LSC 10	0.072	5.51	0.15	5.61
LSC 20	0.059	5.54	0.14	5.67
LSC 30	0.055	5.59	0.10	5.71
LSC40	0.057	5.54	0.13	5.70
LSCM 10	0.19	5.81	0.14	4.86
LSCM 20	0.18	5.88	0.13	5.77
LSCM 30	0.17	5.98	0.10	5.88
LSCM40	0.18	5.99	0.12	5.81
LCC 10	0.19	6.29	0.14	5.15
LCC 20	0.18	6.39	0.13	5.16
LCC 30	0.17	6.71	0.10	5.28
LCC40	0.19	6.54	0.12	5.20

The same theoretical exponential temperature dependency of conductivity and magnitude increase in function of Ca content was evidenced in experimental results as presented in Fig.7c; for the Ca doped system, the electrical conductivity trends and behavior of DFT modelling and experimental measurements agreed.

Fig. 14a shows bar plots representing the trends in the normalized activation energy difference of electrical conductivity as a function of the substituent cation concentration difference obtained theoretically and experimentally for LSC*x*, LSCM*x* and LCC*x* within the rhombohedral phase region. The x-axis (both lower and upper x-axis labels) refers to the label assigned to the difference between two substituent cation concentration levels, where i and j are the index for the concentration differences from the DFT modeling (represented by the red bars) and the experimental concentrations (represented by the blue bars), respectively. Table S1 in supplementary section summarizes the different labels for each of the concentration differences, as well as the value of the normalized activation energy differences. The labels $\Delta C_i;\ i = 1\ -3$ refer to the differences between the activation energies between LSC8.3-LSC16, LSC16-LSC25 and LSC8.3-LSC25, respectively.

The difference between the activation energies increases between ΔC_1 and ΔC_2; however, it decreases at ΔC_3 due to the greater difference between the concentrations. It can be clearly observed how the theoretical behavior agrees with the trend of the differences in activation energies obtained experimentally ($\Delta C_j;\ j = 1 - 3$; that represent the activation energies differences between LSC10-LSC20, LSC20-LSC30 and LSC10-LSC30). The magnitude of the experimental differences is underestimated compared to the results of the DFT modeling. The labels $\Delta C_i;\ i = 4 - 9$ refer to the differences between the activation energies between LSCM8.3-LSCM16, LSCM16-LSCM25, LSCM8.3-LSCM25, LCC8.3-LCC16, LCC16-LCC25 and LCC8.3-LCC25, respectively.

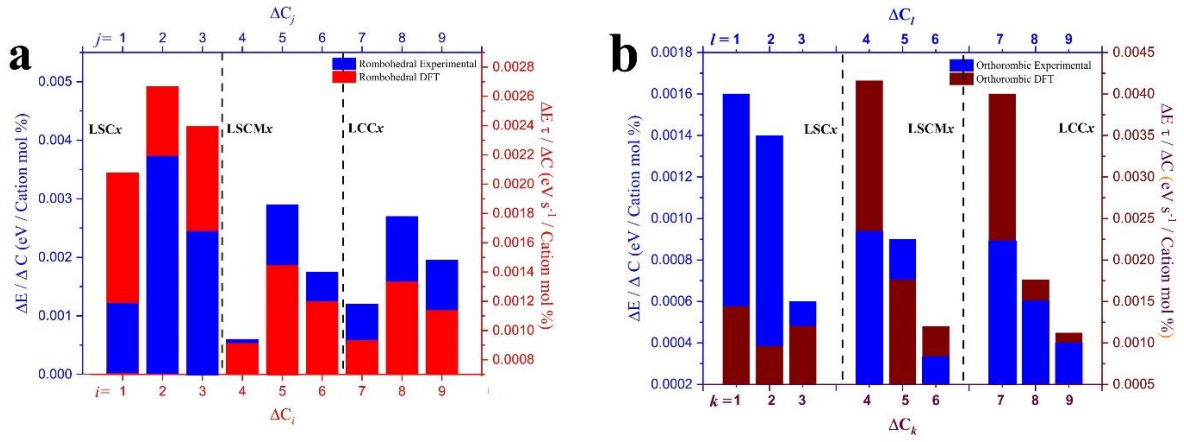

Fig 14 Normalized activation energy difference relative to substituent concentration level difference for **(a)** rhombohedral phase (high temperature region) and **(b)** orthorhombic phase (low temperature region).

For each data set (LSCM*x* and LCC*x*), the same trend is observed between the differences in the activation energy observed in the LSC*x* set; however, in all cases, the magnitude of said difference is underestimated in relation to the experimental trends.

Although the initial interest of the present study was to investigate the effects of the substituent concentration on the behavior of the electrical conductivity at high temperature, and therefore only on rhombohedral phase region, the current work also reviewed the lower temperature orthorhombic phase region. The orthorhombic phase *valid region* was assumed in this work to be ≤30 ºC, ≤260 ºC and ≤306 ºC for LSC*x*, LSCM*x* and LCC*x*, respectively. Fig.13d-f shows the temperature dependence of the electrical conductivity for the DFT modelling where the orthorhombic phase was used for all calculations. Fig 13.d shows the LSC*x* (x=12.5%, 25%, 37.5%) exponential trend of (σ/τ) below 30 ºC (within the *valid region* for this phase). An increase in conductivity was observed when the Sr content increased from LSC12.5 to LSC25; however, when the strontium molar content increased up to 37.5 %, a drop in the electrical conductivity was observed. Theoretically, this drop indicates a higher oxygen vacancy concentration and a decrease in electrical conductivity, as proposed by [75]. As cited before, DFT modelling predicts an exponential trend in this valid region that was not observed in the experimental results. The experimental anomalous trend can be associated with the phase transition, and mobility of Sr, that leads to the formation of the strontium chromate secondary phase. The DFT method used was not able to predict the formation of a secondary phase, and the effect on the electrical conductivity behavior for the LSC*x* structure.

In the same way, Fig. 13.e and Fig.13.f shows the (σ/τ) dependence with temperature for LSCM*x* and LCC*x* (x=12.5%, 25%, 37.5%) in the *valid regions* for the orthorhombic phase for each data set. The DFT theoretical model predicts a semiconductor exponential behavior for all substitutions levels. The electrical conductivity increased proportionally with Mn and Ca content between the 12.5 % and 25.0 %. Increasing the substituent content up to 37.5 % predicted a decrease in

conductivity. For the Mn substitution, this fact is justified by the increase in the Mn^{+3} to Mn^{+4} transition that interferes with polaron formation in chromium sites. Fig.15 shows a magnified area of the orthorhombic phase valid region for the theoretical and experimental electrical conductivity trends for LCC*x* compositions. This figure shows in detail the increase in electrical conductivity with the increase in Ca content. Theoretical calculations supported that the increase of divalent dopants at high substitution levels (≥37.5 %) produced oxygen vacancy formation and the electrical conductivity decrease observed. The modelling results agreed with the experimental results reported by Liu *et al.* [83]. In summary, both the LCC*x* and LSCM*x* electrical conductivity exponential trends agreed with those observed in the experimental results for the orthorhombic phase.

As described for the DFT-experimental data comparison for the rhombohedral phase in Fig. 14a, Fig. 14b shows the bar plots representing the trends in the normalized activation energy difference as a function of the substituent cation concentration difference for the DFT modeling (shown in brown bars) and the experimental results (shown in blue bars) obtained for LSC*x*, LSCM*x* and LCC*x* in the temperature region of orthorhombic phase presence. The labels ΔC_k and ΔC_l, where k and $l = 1 - 9$, refer to the theoretical and experimental activation energies differences, respectively (see labels definition in Table S.1). In this figure, a clear decreased tendency between the experimental activation energies differences for each Sr, Ca and Sr/Mn doped $LaCrO_3$ sub-sets is shown. The general observed pattern shows that the highest activation energy difference occurs generally between the 10% and 30% of substituent concentration (for ΔC_k and ΔC_l; where k and $l = 1, 4$ and 7); meaning that at the low temperatures regime where the orthorhombic phase predominates, this 20% increase of cations substituents has more impact in the electrical conductivity improvement, relative to the other normalized differences. In the same way, it also can be observed that for the difference between 30% and 40% of substituent concentration (for ΔC_k and ΔC_l; where k and $l = 2, 5$ and 8) such difference is smaller, indicating that this 10% increase between these higher substitution levels does not increase the conductivity magnitude significantly. The DFT modelling determined the activation energy differences trends, which were similar as the experimental trends, where the highest differences occur for ΔC_k and ΔC_l, and k and $l = 1, 4$ and 7. This indicates that a 20% content increase between these two concentration levels increases the electrical conductivity of the doped $LaCrO_3$ proportionally. For the LSC*x* set, the DFT difference trends were different to the experiments and the values were underestimated. As explained before, the DFT modelling used did not predict the mobility of Sr ions at higher temperatures and the potential formation of secondary phases as evidenced in the experiments. However, for LSCM*x* and LCC*x* sets, the DFT trends show the same decrease trend between substituent concentration difference as observed on the experiments. However, in these two sets, the activation energies magnitudes were overestimated by the calculation model used. The LCC*x* modelling was more accurate in comparison with the other two doped $LaCrO_3$ compositions relative to the experimental results.

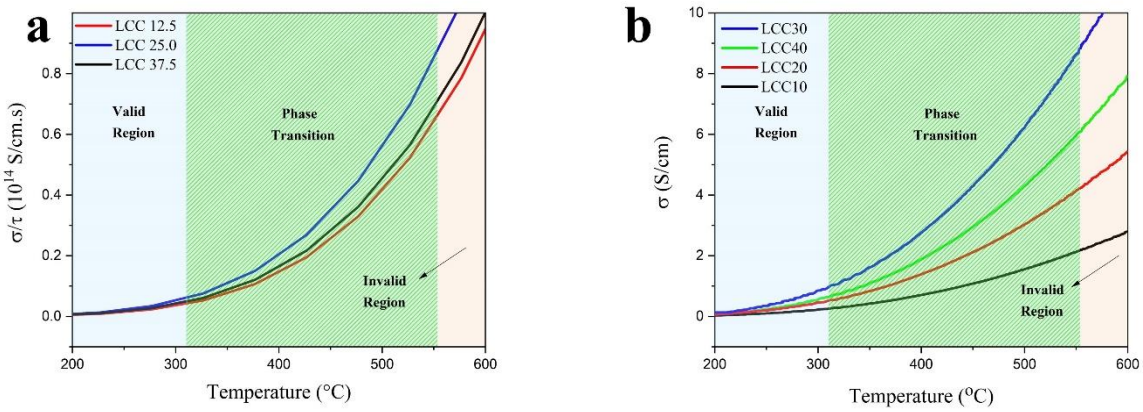

Fig 15 (a) DFT theoretical (σ/τ) and **(b)** experimental electrical conductivity (right) dependence with temperature of orthorhombic crystalline (low temperature) structures for LCC*x*.

When comparing the trends in the DFT calculations for the activation energies between the orthorhombic and rhombohedral phases (in the *valid regions*) for LSC*x*, LSCM*x* and LCC*x*, it can be observed in Table 5, in general, the electrical conductivity activation energies for the orthorhombic phase display greater magnitude than those reported for the rhombohedral phase. This follows the known correlation of higher symmetry with a general increase in carrier mobility, and thus, relative increase in conductivity [84, 85]. In addition, even though lattice ordering may be affected by the increased dopant addition, the symmetry appears to increase with increased dopant substitution with the tolerance factor approaching 1. Table 1 shows that with an increase in Sr content within the LSC*x* material, the tolerance factor tends towards 1, indicating the formation of a higher symmetry rhombohedral phase at lower temperatures. Hence, the transition temperature decreases with the Sr content compared to pure $LaCrO_3$. In the same way, as the content of Sr/ Mn is increased within the LSCM*x* material, the value of the tolerance factor approaches 1, indicating further movement towards the rhombohedral phase. However, in the case of Ca, the increase in the cation concentration inversely influences the tolerance factor, that is, increasing the amount of Ca reduces the magnitude of the tolerance factor. This indicates that the orthorhombic to rhombohedral transition temperature increases [86]. The further incorporation of the cation substituent enhances the crystalline symmetry producing a larger overlap between O-2p and Cr-3d orbitals, which enhances the charge carrier exchange and is expected to be optimal when the Cr-O bond length is smaller [87].

5. Conclusions

Doped lanthanum chromite compositions (with Sr and Ca doping on the A-site and Mn doping on the B-site up to a doping level of 40%) were prepared by a Pechini sol-gel method. High density polycrystalline ceramics from these powders were produced using a reactive sintering methodology. The lattice parameters were determined by XRD measurements using Rietveld

analysis. The increase in dopant concentration resulted in the expected decrease in the lattice parameter and unit cell volume magnitude due to the chromium ion oxidation and oxygen vacancy formation.

The electrical conductivity for the different doped lanthanum chromite materials were acquired up to 1500 ^{o}C for the first time. The electrical conductivity trends were shown to be exponential in behavior in dry air for the Ca-doped and the Sr/Mn co-doped chromites, and the measurements for these two compositional sets were relatively stable. Generally, the electrical conductivity increased as a function of doping level up to 30 % for all dopants (Sr^{+2}, Ca^{+2}, Mn^{+3}). In addition, the increase in cation substitution improved densification of bulk materials, enhancing in this way the electrical conductivity to temperatures up to 1500 ^{o}C. Unlike the Ca- and Sr/Mn-doped compositions, the Sr-doped lanthanum chromites deviated from the exponential behavior. It was observed that Sr solubility limit was reached between 800 ^{o}C to 1100 ^{o}C, which resulted in the strontium chromate secondary phase formation. The precipitation of this secondary phase resulted in the anomalous conductivity observed trend. It is important to highlight that the Sr/Mn system did not show the same secondary phase as the pure Sr-doped samples, and this co-doped system maintained the expected exponential conductivity trend with increasing temperature. The same compositions were tested under reducing atmosphere from 600 to 1500 ^{o}C and pO_2 atmospheres $\leq 10^{-14}$ atm. The conductivity showed a relatively strong dependence on the oxygen pressure and its magnitude decreased due to ionic compensation, where the formation of oxygen vacancies was the dominant mechanism at the lower pO_2 levels. It was observed that at lower working temperatures and low pO_2, the electrical conductivity showed higher values, however increasing the temperature the ionic conduction was more notable due faster oxygen vacancies formation.

In addition, an improved DFT theoretical model was developed in order to understand the effect of different divalent and trivalent cations substitution in the A- and B-site of lanthanum chromite perovskites on their structural and electrical properties at high temperatures. The initial calculations, following modelling protocols used by previous authors, resulted in materials showing metallic behavior that did not agree with the experimental observations reported in this and other works. The DFT modelling approach was altered through the insertion of oxygen vacancies, resulting in the expected trends for the physical properties that could be contrasted with experimental results. With this corrected and improved theoretical DFT model, the structural properties were determined, such as the lattice parameters and unit cell volume for the orthorhombic crystalline structure (for the room temperature phase). It was found that increasing the cation substituent percentages in the lanthanum chromite perovskite resulted in a decrease in the lattice parameters magnitudes as observed in the experimental XRD analysis.

Both the orthorhombic and rhombohedral phases were included for the DFT estimation of the conductivity properties for the various doped-chromites, due to the orthorhombic-rhombohedral phase transition at temperatures ≥600 K. To better understand the phase transition influence on electrical properties, a set of calculations were performed to determine the temperature dependence of (σ/τ) up to 1500 ^{o}C for the LSC*x*, LSCM*x* and LCC*x* compositions. The simultaneous consideration of each phase was not previously reported while estimating the physical properties of the doped $LaCrO_3$ compositions. It must be stated though that the rhombohedral phase properties

were considered more relevant for the results of this work due to the proposed high-temperature sensor application. The DFT modeling predicted an exponential trend for the temperature dependence of (σ/τ) in all compositions as compared with the conductivity experimental results, except for the Sr-doped compositions. The "relative" activation energies of both experimental and theoretical data were calculated from the Arrhenius plots. The DFT and experimental data showed similar trends for all the compositions sets, except for the Sr-doped composition due to the anomaly within the experimental data as a result of the $SrCrO_3$ second phase formation. Since the compositions studied between the modeling and experiments were not similar (due to modelling restrictions), the activation energies could not be directly compared. Instead, the change of activation energies as a function of composition change (dopant content difference) was compared between the modelling and experiments in order to normalize the data in some fashion. The DFT calculations showed that increasing the content of Sr or Ca on the A- and Mn on the B-site up to percentages close to 30% resulted in the increase of the (σ/τ) magnitude, as observed similarly in the experimental measurements in the temperature region where the rhombohedral phase predominates. This work unveils the potential of doped lanthanum chromites for high-temperature applications, offering insights into their structural and electrical properties for advancing materials in extreme conditions.

6. Acknowledgments

This work is supported by the United States Department of Energy (DOE) through the research project grant (DE-FE0031825). The authors would also like to acknowledge the technical support of Dr. Qiang Wang and Dr. Marcela Redigolo of West Virginia University and the entire WVU Shared Research Facilities (SRF) for assistance in characterization and technical input. All the DFT calculations reported in this work were performed using GRANADO HPC facilities at Universidad del Norte, Colombia.

7. References

[1] H. Tamura, H. Yoneyama, Y. Matsumoto, in: S. Trasatti (Ed.), Electrodes of Conductive Metallic Oxides. Part A, Elsevier, Amsterdam, 1981.

[2] M. Rubel, T. Takei, N. Kumada, M. M. Ali, A. Miura, K. Tadanaga, K. Oka, M. Azuma, M. Yashima, K. Fujii, E. Magome, C. Moriyoshi, Y. Kuroiwa, J. H. Maxim, Hydrothermal Synthesis, Crystal Structure, and Superconductivity of a Double-Perovskite Bi Oxide. *Chemistry of Materials* 28 (2) (2016) 459-465 https://doi.org/10.1021/acs.chemmater.5b02386

[3] A.S. Moskvin, N.S. Ovanesyan, V.A. Trukhtanov, Angular dependence of the superexchange interaction iron(3+)-oxygen(2-)-chromium (3+), *Hyperfine Interactions* 1 (4) (1975) 265–281.

[4] G. Martinelli, M.C. Carotta, E. Traversa, G. Ghiotti, Thick-film gas sensors based on nano-sized semiconducting oxide powders, *Mater. Res. Soc. Bull*. 24 (6) (1999) 30 – 35.

[5] C. Torres-Garibay, D. Kovar, A. Manthiram, Ln0.6Sr0.4- Co1−yFeyO3−δ. (Ln=La and Nd; y=0 and 0.5) cathodes with thin yttria-stabilized zirconia electrolytes for intermediate temperature solid oxide fuel cells, *Journal of Power Sources* 187 (2) (2009) 480–486.

[6] N. Zarrin, S. Husain, Study of structural, morphological, optical, and dielectric behavior of zinc-doped nanocrystalline lanthanum chromite. *Appl. Phys. A* 124 (2018) 730.

[7] O. Polat, Z. Durmus, F.M. Coskun, M. Coskun, A. Turut, Engineering the band gap of $LaCrO_3$ doping with transition metals (Co, Pd, and Ir), *J. Mater. Sci.* 53 (2018) 3544–3556.

[8] M. Mori, Y. Hiei, T. Yamamoto, Control of the Thermal Expansion of Strontium-Doped Lanthanum Chromite Perovskites by B-site Doping for High-Temperature Solid Oxide Fuel Cell Separators. *Journal of the American Ceramic Society* 84 (2001) 781-786.

[9] M. Cokun, O. Polat, F.M. Coskun, Z. Durmus¸, M. Çaglar, A. Türüt, Frequency and temperature dependent electrical and dielectric properties of $LaCrO_3$ and Ir doped $LaCrO_3$ perovskite compounds, *J. Alloys Compd.* 740 (2018) 1012–1023.

[10] J. Sfeir, P. A. Buffat, P. Möckli, N. Xanthopoulos, R. Vasquez, H. J. Mathieu, J. V. Herle, K. R. Thampi, Lanthanum Chromite Based Catalysts for Oxidation of Methane Directly on SOFC Anodes, Journal of Catalysis, 202 (2) (2001) 229-244. https://doi.org/10.1006/jcat.2001.3286.

[11] W.Z. Zhu, S.C. Deevi, Development of interconnect materials for solid oxide fuel cells, *Materials Science and Engineering: A* 348 (2003) 227-243. https://doi.org/10.1016/S0921-5093(02)00736-0.

[12] S. Hussain, M. S. Javed, N. Ullah, A. Shaheen, N. Aslam, I. Ashraf, Y. Abbas, M. Wang, G. Liu, G. Qiao, Unique hierarchical mesoporous $LaCrO_3$ perovskite oxides for highly efficient electrochemical energy storage applications, *Ceramics International* 45 (2019) 15164-15170. https://doi.org/10.1016/j.ceramint.2019.04.258.

[13] D. Liu, P. Shi, W. Ren et al. Facile high-performance film thermocouple made of strontium lanthanum chromate for temperature sensing in air. *J Am Ceram Soc*. 101 (2018) 4880– 4886. https://doi.org/10.1111/jace.15878.

[14] K. Hilpert, R.W. Steinbrech, F. Boroomand, E. Wessel, F. Meschke, A. Zuev, O. Teller, H. Nickel, L. Singheiser, Defect formation and mechanical stability of perovskites based on $LaCrO_3$ for solid oxide fuel cells (SOFC), *J. Eur. Ceram. Soc*. 23 (2003) 3009–3020.

[15] T. Akashi, T. Maruyama, T. Goto. Transport of lanthanum ion and hole in $LaCrO_3$ determined by electrical conductivity measurements, *Solid State Ionics*, 164 (2003) 177-183.

[16] Q. Hui, L. Yongxin, C. Songtian, Z. Ling, Z. Xudong, H. Changmin, Preparation, characterization and electrical properties of Ca and Sr doped $LaCrO_3$, *Inorg. Chem. Commun*. 66 (2016) 33–35.

[17] K. P. Bansal, S. Kumari, B. K. Das, G. C. Jain, On some transport properties of strontium-doped lanthanum chromite ceramics. *Journal of Materials Science* 18 (1983) 2095-2100.

[18] M. Mori, T. Yamamoto, T. Ichikawa, Y. Takeda. Dense sintered conditions and sintering mechanisms for alkaline earth metal (Mg, Ca and Sr)-doped LaCrO3 perovskites under reducing atmosphere, Solid State Ionics 148 (2002) 93-101.

[19] É.P., Marinho, A.G. Souza, D.S. de Melo, *et al.* Lanthanum chromites partially substituted by calcium, strontium and barium synthesized by urea combustion. *J Therm. Anal. Calorim.* 87, (2007) 801–804. https://doi.org/10.1007/s10973-006-7877-7.

[20] H.P.S Correa, C.O Paiva-Santos, L.F. Setz, L.G Martinez, S.R.H. Mello-Castanho. M.T.D. Orlando. Crystal structure refinement of Co-doped lanthanum chromites. *Powder Diffr. Suppl*. 23 (2008) 18-22.

[21] S.M. El-Sheikh, M.M. Rashad, Effect of Sm3+ and Sr2+ dopants on the FT-IR, photoluminescence and surface texture of lanthanum chromite nanoparticles, *Journal of Alloys and Compounds*, 496 (2010), 723-732. https://doi.org/10.1016/j.jallcom.2010.03.061.

[22] W. Hu, Y. Chen, H. Yuan, G. Zhang, G. Li, G. Pang, S. Feng. Hydrothermal synthesis, characterization and composition-dependent magnetic properties of LaFe1−xCrxO3 system (0≤x≤1). *Journal of Solid State Chemistry* 183 (2010) 1582-1587. https://doi.org/10.1016/j.jssc.2010.04.041

[23] D. Berger, I. Jitaru, N. Stanica *et al.* Complex Precursors for Doped Lanthanum Chromite Synthesis. *Journal of Materials Synthesis and Processing* 9 (2001) 137–142. https://doi.org/10.1023/A:1013297430679.

[24] N. Zarrin, S. Husain. Study of structural, morphological, optical, and dielectric behavior of zinc-doped nanocrystalline lanthanum chromite. *Appl. Phys. A* 124 (2018) 730. https://doi.org/10.1007/s00339-018-2139-7

[25] Z. Yang, K.S. Weil, D.M. Paxton, J.W. Stevenson, Selection and Evaluation of Heat-Resistant Alloys for SOFC Interconnect Applications, *J. Electrochem. Soc.*, 150 (2003) A1188-A1201.

[26] W.J. Weber, C.W. Griffin, J.L. Bates, Effects of cation substitution on electrical and thermal transport properties of $YCrO_3$ and $LaCrO_3$, *J. Am. Ceram. Soc.* 70 (1987) 265 – 270.

[27] M. Mori, T. Yamamoto, H. Itoh, T. Watanabe, Compatibility of alkaline earth metal (Mg, Ca, Sr)-doped lanthanum chromites as separators in planar-type high-temperature solid oxide fuel cells. *Journal of Materials Science* 32 (1997) 2423–2431 https://doi.org/10.1023/A:1018565409603.

[28] M. Mori, Y. Hiei, N. M. Sammes, Sintering behavior and mechanism of Sr-doped lanthanum chromites with A site excess composition in air, Solid State Ionics 123 (1999) 103-111. https://doi.org/10.1016/S0167-2738(99)00097-1.

[29] T. Armstrong, J. Stevenson, L. Pederson, P. Raney, Dimensional Instability of Doped Lanthanum Chromite, *J. Electrochem. Soc.* 143 (1996) 2919-2925.

[30] N. Sakai, H. Yokokawa, T. Horita, K. Yamaji. Lanthanum Chromite-Based Interconnects as Key Materials for SOFC Stack Development, *International Journal of Applied Ceramic Technology* 1 (2004) 23-30. https://doi.org/10.1111/j.1744-7402.2004.tb00151.x

[31] S. Jiang, L. Zhangab, Y. Zhangb. Lanthanum strontium manganese chromite cathode and anode synthesized by gel-casting for solid oxide fuel cells, *J. Mater. Chem.* 17 (2007) 2627-2635.

[32] J. Furtado, R.N. Oliveira, Development of Lanthanum Chromites-Based Materials for Solid Oxide Fuel Cell Interconnects, *Matéria.* 13 (2008) 147-153.

[33] W.Z. Zhu, S.C. Deevi, Development of interconnect materials for solid oxide fuel cells, *Materials Science and Engineering: A* 348 (2003) 227-243 https://doi.org/10.1016/S0921-5093(02)00736-0.

[34] N. Q. Minh, Ceramic Fuel Cells, *J. Am. Ceram. Soc.*, 76 (1993) 563–88.

[35] S. Gupta, Y. Zhong, M. Mahapatra, P. Singh, Processing and electrochemical performance of manganese-doped lanthanum-strontium chromite in oxidizing and reducing atmospheres, *International Journal of Hydrogen Energy*, 40 (2015) 13479-13489. http://doi.org/10.1016/j.ijhydene.2015.07.153

[36] L. Lutterotti, S. Matthies, H.R. Wenk, MAUD: a friendly Java program for material analysis using diffraction, IUCr Newsl. CPD 21 (1999) 14–15.

[37] J.P. Perdew, K. Burke, M. Ernzerhof, Generalized gradient approximation made simple, *Phys. Rev. Lett.* 77 (1996) 3865–3868.

[38] A. M. Deml, V. Stevanovic, C. L. Muhich, C. B. Musgrave, R. O'Hayre; Oxide enthalpy of formation and band gap energy as accurate descriptors of oxygen vacancy formation energetics; *Energy Environ. Sci.* 7 (2014) 1996-2004.

[39] T. A. Mellan, F. Corà, R. Grau-Crespo, S. Ismail-Beigi, Importance of anisotropic Coulomb interaction in $LaMnO_3$; *Phys. Rev, B* 92 (2015) 085151.

[40] T. Hashimoto, K. Takagi, K. Tsuda, M. Tanaka, K. Yoshida, H. Tagawa, M. Dokiya. Theoretical Solution Energy of Alkaline Earth Ions in Lanthanum Chromites. *J. Electrochem. Soc.* 147 (2000) 4408.

[41] T. Hashimoto, N. Tsuzuki, A. Kishi, K. Takagi, K. Tsuda, M. Tanaka, K. Oikawa, T. Kamiyama, K. Yoshida, H. Tagawa, M. Dokiya. Analysis of crystal structure and phase transition of LaCrO3 by various diffraction measurements. *Solid State Ionics* 132 (2000) 181.

[42] Y. Matsunaga et al. Analysis of structural and magnetic phase transition behaviors of La1−*x*Sr*x*CrO3 by measurement of heat capacity with thermal relaxation technique. *Thermochim. Acta*, 474 (2008) 57-61.

[43] Y. Matsunaga et al. Analysis of relationship between magnetic property and crystal structure of La1− xSrxCrO3 (x= 0.13, 0.15). *Solid State Commun*. 145 (2008) 502-506.

[44] F. Nakamura et al. Analysis of magnetic and structural phase transition behaviors of La1− xSrxCrO3 for preparation of phase diagram. *Thermochim. Acta*. 435 (2005) 222-229.

[45] T. Hashimoto, K. Takagi, K. Tsuda, M. Tanaka, K. Yoshida, H. Tagawa, M. Dokiya. Theoretical Solution Energy of Alkaline Earth Ions in Lanthanum Chromites. *J. Electrochem. Soc.* 147 (2000) 4408.

[46] T. Hashimoto, N. Tsuzuki, A. Kishi, K. Takagi, K. Tsuda, M. Tanaka, K. Oikawa, T. Kamiyama, K. Yoshida, H. Tagawa, M. Dokiya. Analysis of crystal structure and phase transition of LaCrO3 by various diffraction measurements. *Solid State Ionics* 132 (2000) 181.

[47] Y. Matsunaga et al. Analysis of structural and magnetic phase transition behaviors of La1− *x*Sr*x*CrO3 by measurement of heat capacity with thermal relaxation technique. *Thermochim. Acta,* 474 (2008) 57-61.

[48] Y. Matsunaga et al. Analysis of relationship between magnetic property and crystal structure of La1− xSrxCrO3 (x= 0.13, 0.15). *Solid State Commun*. 145 (2008) 502-506.

[49] F. Nakamura et al. Analysis of magnetic and structural phase transition behaviors of La1− xSrxCrO3 for preparation of phase diagram. *Thermochim. Acta*. 435 (2005) 222-229.

[50] N. Ohba et al. Analysis of the Effect of the Oxide Ion Vacancy on the Crystal Structure of $La_{1-x}Ca_xCrO_{3-\delta}$ by High-Temperature X-Ray Diffraction under Various Oxygen Partial . *Defect and Diffusion Forum.* 242-244 (2005) 9-16.

[51] P.E. Bloch. Projector augmented-wave method, *Phys. Rev. B* 50 (1994) 17953–17979.

[52] X. Liu, W. Su, Z. Lu, J. Liu, L. Pei, W. Liu, L. He. Mixed valence state and electrical conductivity of La1−xSrxCrO3, Journal of Alloys and Compounds. V 305. (2000) 21-23. https://doi.org/10.1016/S0925-8388(00)00735-0.

[53] S. Wang, K. Huang, B. Zheng, J. Zhang, S. Feng, Mild hydrothermal synthesis and physical property of perovskite Sr doped LaCrO3, *Materials Letters*. V 101, (2013) 86-89, https://doi.org/10.1016/j.matlet.2013.03.083.

[54] R.D. Shannon, Revised effective ionic radii and systematic studies of interatomic distances in halides and chalcogenides, *Acta Crystallogr. A* 32 (1976) 751 – 767.

[55] B. H.Choi, S. Park, B. K. Park, H. H. Chun, Y. Kim, Controlled synthesis of La1−xSrxCrO3 nanoparticles by hydrothermal method with nonionic surfactant and their ORR activity in alkaline medium, *Materials Research Bulletin*, 48 (2013) 3651-3656. https://doi.org/10.1016/j.materresbull.2013.04.084.

[56] J. W. Fergus, Lanthanum chromite-based materials for solid oxide fuel cell interconnects, *Solid State Ionics* 171 (2004) 1-15. https://doi.org/10.1016/j.ssi.2004.04.010.

[57] J.C. Rendón-Angeles, K. Yanagisawa, Z. Matamoros-Veloza, M.I. Pech-Canul, J. Mendez-Nonell, S. Diaz-de la Torre, Hydrothermal synthesis of perovskite strontium doped lanthanum chromite fine powders and its sintering, *Journal of Alloys and Compounds* 504 (2010) 251-256. https://doi.org/10.1016/j.jallcom.2010.05.103.

[58] R. Koc, H. U. Anderson, S. A. Howard, D. M. SParlin. "Proceedings of the First International Symposium on SOFC, Florida", edited by S. C. Singhal (The Electro- , chemical Society Inc., Pennington, N J, 1989) p. 220.

[59] Y. Song, Q. Zhong, W. Tan. Synthesis and electrochemical behavior of ceria-substitution LSCM as a possible symmetric solid oxide fuel cell electrode material exposed to H2 fuel containing H2S. International Journal of Hydrogen Energy. V 39 (2014) 13694-13700. https://doi.org/10.1016/j.ijhydene.2014.03.179

[60] H .Xiong, G.J Zhang, J.Y Zheng, Y.Q Jia. Synthesis, crystal structure and electric conductivity of La0.9Ca0.1Cr0.5B0.5O3 (B=Mn, Fe, Ni). *Materials Letters*. V 51 (2001) 61-67. https://doi.org/10.1016/S0167-577X(01)00265-8

[61] G. Li, X. Chen, Y. Liu, Y. Chen, W. Yang. One-time sintering process to synthesize ZrO_2-coated $LiMn_2O_4$ materials for lithium-ion batteries. *RSC Adv*. 8 (2018) 16753.

[62] S. Mukherjee, M. Gonal, M. Patel, M. Roy, A. Patra, A.K. Tyagi. Microstructure Characterization and Electrical Conductivity Measurement of La1-xCaxCrO3 (x=0.25, 0.4, 0.5) Prepared by Aspartic Acid-Assisted Solution Combustion. *Journal of the American Ceramic Society*. 95. (2012). 290-295.

[63] L.P. Rivas-Vázquez, J.C. Rendón-Angeles, J.L. Rodríguez-Galicia, C.A. Gutiérrez-Chavarria, K.J. Zhu, K. Yanagisawa, Preparation of calcium doped LaCrO3 fine powders by hydrothermal method and its sintering, *Journal of the European Ceramic Society* 26 (2006) 81-88. https://doi.org/10.1016/j.jeurceramsoc.2004.10.023.

[64] L.P. Rivas-Vázquez, J.C. Rendón-Angeles, J.L. Rodríguez-Galicia, K. Zhu, K. Yanagisawa, Hydrothermal synthesis and sintering of lanthanum chromite powders doped with calcium, Solid State Ionics 172 (2004) 389-392. https://doi.org/10.1016/j.ssi.2004.03.021.

[65] A. R. Denton, N. W. Ashcroft, "Vegard's law," Phys. Rev. A 43 (1991) 3161–3164.

[66] K. Maiti, D. D. Sarma, Electronic structure of $La_{1-x}Sr_xCrO3$, *Phys Rev B Condens Matter*. 54 (1996)7816-7822.

[67] H. Yokokawa, N. Sakai, T. Kawada, M. Dokiya, Thermodynamic stabilities of perovskite oxides for electrodes and other electrochemical materials, *Solid State Ionics* 52 (1992) 43-56.

[68] S. Simner, J. Hardy, J. Stevenson, Sintering mechanisms in strontium doped lanthanum chromite. *Journal of Materials Science* 34 (1999) 5721–5732. https://doi.org/10.1023/A:1004745915378

[69] T. R. Armstrong, J. W. Stevenson, K. Hasinska, D. E. McCready, Synthesis and Properties of Mixed Lanthanide Chromite Perovskites, *J. Electrochem. Soc.* 145 **(**1998) 4282.

[70] G .H. Jonker, Semiconducting properties of mixed crystals with perovskite structure, *Physica* 20 (1954) 1118-1122. https://doi.org/10.1016/S0031-8914(54)80250-3.

[71] D.B. Meadowcroft, Some properties of strontium-doped lanthanum chromite, *J. Phys. D: Appl. Phys.* 2 (1969) 1225-1233.

[72] J.D. Carter, M.M. Nasrallah, H.U. Anderson, Liquid phase behavior in nonstoichiometric calcium-doped lanthanum chromites. *Journal of Materials Science* 31 (1996)157–163.

[73] Z. Cai, M. Jiang, Q. Guo, X. Jiang, S. Chen, H. Sun, Effect of applied pressure on microstructure and properties of hot-pressed Ca-doped LaCrO3 ceramics, *International Journal of Applied Ceramic Technology,* 18 (2021) 684-696.

[74] M.W. Barsoum. Fundamentals of Ceramics IOP Publishing Ltd., United Kingdom (2003) pp. 328–334.

[75] P. Devi, M. Rao, Preparation, structure, and properties of strontium-doped lanthanum chromites: La1−xSrxCrO3, *Journal of Solid State Chemistry* 98 (1992) 237-244. https://doi.org/10.1016/S0022-4596(05)80231-2.

[76] D.H. Peck, M. Miller, K. Hilpert, Phase diagram studies in the SrO–Cr2O3–La2O3 system in air and under low oxygen pressure, *Solid State Ionics* 123 (1999) 59-65, https://doi.org/10.1016/S0167-2738(99)00088-0.

[77] J. Weber, W. Griffin, L. Bates, Effects of Cation Substitution on Electrical and Thermal Transport Properties of $YCrO_3$ and $LaCrO_3$. *Journal of the American Ceramic Society*, 70 (1987) 265-270. https://doi.org/10.1111/j.1151-2916.1987.tb04979.x

[78] J.B. Webb, M. Sayer, A. Mansingh, Polaronic Conduction in Lanthanum Strontium Chromite, *Can. J. Phys*., 55 (1977) 1725.

[79] G. Stakkestad, S. Faaland, T. Sigvartsen, Investigation of electrical conductivity and seebeck coefficient of Ca-and Sr-doped $LaCrO_3$, *Phase Transitions: A Multinational Journal,* 58 (1996) 159-173.

[80] N. Sakai, T. Kawada, H. Yokokawa, Sinterability and electrical conductivity of calcium-doped lanthanum chromites. *J Mater Sci* 25 (1990) 4531–4534. https://doi.org/10.1007/BF00581119

[81] J. Mizusaki, S. Yamauchi, K. Fueki, A. Ishikawa, Nonstoichiometry of the perovskite-type oxide La1−xSrxCrO3−δ, Solid State Ionics 12 (1984) 119-124. https://doi.org/10.1016/0167-2738(84)90138-3.

[82] P. Khuong, O. Wu, P. Wu; Optimization of electrical conductivity of $LaCrO_3$ through doping: A combined study of molecular modeling and experiment; *Appl. Phys. Lett.* 90 (2007) 044109/1-044109/3.

[83] X. Liu, W. Su, Z. Lu, J. Liu, L. Pei, W. Liu, L. He, Mixed valence state and electrical conductivity of $La_{1-x}Sr_xCrO$; *Journal of Alloys and Compounds* 305 (2000) 21–23.

[84] E. Niwa, T. Sato, Y. Watanabe, Y. Toyota, Y. Hatakeyama, K. Judai, K. Shozugawa, M. Matsuo, T. Hashimoto. Dependence of crystal symmetry, electrical conduction property and electronic structure of LnFeO3 (Ln: La, Pr, Nd, Sm) on kinds of Ln3+. *Journal of the Ceramic Society of Japan*. 123. (2015) 501-506.

[85] A. Mineshige, M. Inaba, T. Yao, Z. Ogumi, K. Kikuchi, M. Kawase. Crystal Structure and Metal–Insulator Transition of La1−xSrxCoO3. *Journal of Solid State Chemistry*. 121, Issue 2. (1996) 423-429. https://doi.org/10.1006/jssc.1996.0058.

[86] S.P. Tolochko, I.F. Kononyuk, V.A. Lyutsko, Yu.G. Zonov. Phase transitions in solid solutions based on lanthanum chromite. *Izv Akad Nauk SSSR, Neorg Mater*, 23(9). (1987) 1520-1524.

[87] S. Gupta, M. K. Mahapatra, P. Singh. Lanthanum chromite based perovskites for oxygen transport membrane. *Materials Science and Engineering: R: Reports*. 90. (2015) 1-36. https://doi.org/10.1016/j.mser.2015.01.001.